JOURNAL OF GEOPHYSICAL RESEARCH, VOL. 112, C06024, doi:10.1029/2006JC003831, 2007

Enhanced turbulence due to the superposition of internal gravity waves and a coastal upwelling jet

G. S. Avicola,[1,2] J. N. Moum,[1] A. Perlin,[1] and M. D. Levine[1]

Received 21 July 2006; revised 4 November 2006; accepted 29 November 2006; published 28 June 2007.

[1] The upwelling-driven coastal jet off Oregon is in geostrophic balance to first order. The accompanying thermal wind shear is stable to shear instability. Yet enhanced turbulence is observed in the upwelling jet, typically as long, thin patches with horizontal to vertical aspect ratios of 10^2 to 10^3 (median value ~300). These patches are clearly defined by regions of low Richardson number and occur where and when the linear superposition of the three dominant shear constituents (near-inertial, M_2, and thermal wind) interferes constructively. This is most pronounced at the base of the coastal jet, where the thermal wind shear is largest. While the effect of the turbulence stress divergence on the jet is small compared to geostrophy (~1%), it is significant in the second-order force balance governing secondary circulation. The timescale associated with the decay of the thermal wind shear via turbulence stress is O(10) days. We confirm that the vertical salt flux due to mixing is comparable to the net Ekman transport of salt onto the shelf within the bottom boundary layer. Because numerical models of coastal circulation lack turbulence in midwater column, any vertical transport of scalars, including salt and heat, must be achieved inshore of the 40-m isobath. This is inconsistent with the observations presented in this study, in which significant vertical turbulent salt transport is found to exist across the entire shelf.

Citation: Avicola, G. S., J. N. Moum, A. Perlin, and M. D. Levine (2007), Enhanced turbulence due to the superposition of internal gravity waves and a coastal upwelling jet, *J. Geophys. Res.*, *112*, C06024, doi:10.1029/2006JC003831.

1. Introduction

[2] During spring and summer off Oregon's coast the wind blows predominantly toward the south. This drives a cross-shelf upwelling circulation which in turn forms a set down in sea surface height and elevated isopycnals at the coast that drive an along-shelf (geostrophically balanced) jet [e.g., *Huyer et al.*, 1978; *Huyer*, 1983]. Maximum jet velocities of 0.4–0.8 m/s are typically located near the 100-m isobath.

[3] In addition to the upwelling jet, there exists an energetic internal gravity wave field. Nonlinear internal waves of elevation [*Klymak and Moum*, 2003; *Moum and Smyth*, 2006; *Moum et al.*, 2007a] and depression [*Moum et al.*, 2003, 2007b] have both been observed on the Oregon shelf: the former during downwelling conditions (winter), the latter during upwelling conditions (summer). Linear internal gravity waves (IGW) also have significant signatures on the shelf [*Denbo and Allen*, 1984]. Baroclinic velocities associated with IGWs of M_2 and near-f frequency (where the descriptor "M_2" refers to the 12.42-hour tidal frequency and "f" refers to the inertial frequency) are reported to be O(0.1) m s^{-1} [*Torgrimson and Hickey*, 1978].

[4] Turbulence in the coastal ocean is generated from a variety of sources, and is a topic of some importance. The transport of scalars (salt, heat, pollutants, nutrients, etc.) depends on both the magnitude and variability of the turbulent mixing. In this study we consider the role of the enhanced shear, from superposition of IGW shear and that of the upwelling jet, in generating turbulence in midwater column. Because numerical models of coastal circulation do not include IGWs, it is particularly important to identify the role that they play in mixing of both scalars and momentum.

[5] Field studies of mixing and turbulence in coastal waters have examined bottom boundary layer dynamics [*Chriss and Caldwell*, 1982; *Dewey and Crawford*, 1988; *Sanford and Lien*, 1999; *Perlin et al.*, 2005a, 2005b], flow around and above topographic features [*Moum and Nash*, 2000; *Nash and Moum*, 2001], the role of turbulent mixing in enhancing cross-shelf exchange [*Dewey et al.*, 1993], and tidally generated turbulence in shallow seas due to tidal straining [*Rippeth et al.*, 2001]. In the latter case, the strain associated with the tidal velocity leads to periods during which the water becomes nearly unstratified, resulting in bottom-to-surface mixing. In addition, *MacKinnon and Gregg* [2003a, 2003b, 2005a, 2005b] examined midwater column turbulence generation in the Mid-Atlantic Bight; in particular, turbulence generation by an IGW field (primarily M_2 and near f) in the absence of a coastal jet. The MacKinnon and Gregg data set provides the most relevant

[1] College of Oceanic and Atmospheric Sciences, Oregon State University, Corvallis, Oregon, USA.
[2] Now at Applied Physics Laboratory, Johns Hopkins University, Laurel, Maryland, USA.

0148-0227/07/2006JC003831$09.00

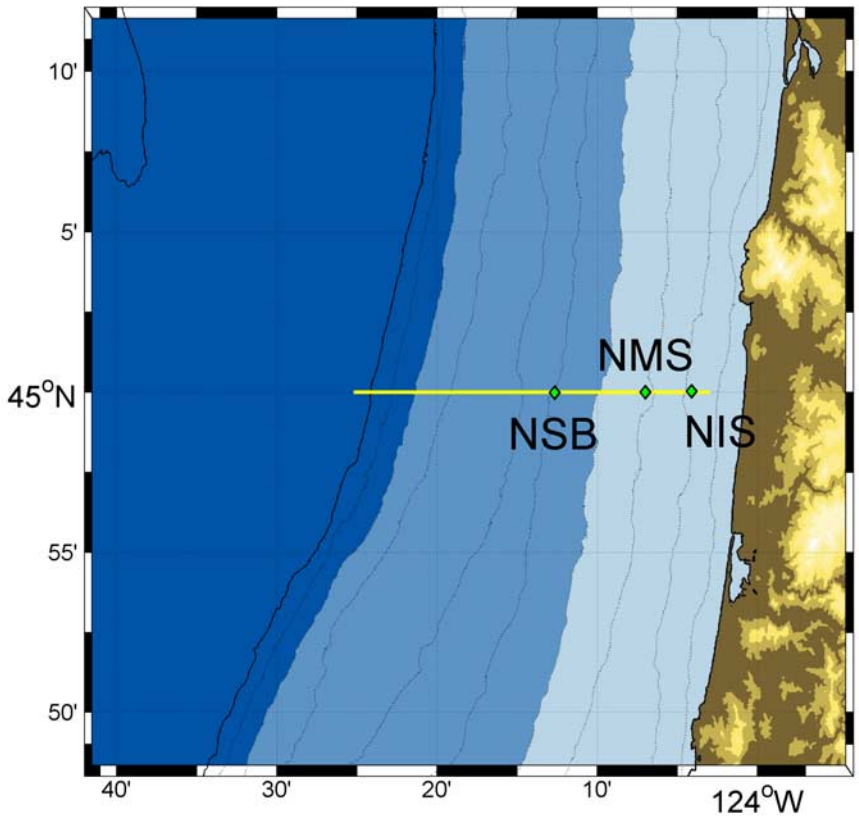

Figure 1. Map of COAST experiment, northern line. Green diamonds indicate the positions of the moorings: NIS (north in shelf) at 50-m depth, NMS (north midshelf) at 80-m depth, and NSB (north shelf break) at 130-m depth. Isobaths are shown with 25-m spacing, the innermost of which is the 25-m isobath. The ship transect line is denoted by the yellow line. Twelve sequential transects were made, moving onshore to offshore.

data set for comparison to this study as they also examine coastal midwater turbulence generation. Their study provides an instructive contrast to ours and is considered in detail by G. S. Avicola et al. (A turbulence parameterization scheme for a coastal internal wave field in the presence of thermal wind shear, submitted to *Journal of Physical Oceanography*, 2006).

[6] The primary goal of this paper is to examine the consequences of the superposition of the internal wave field and a geostrophic jet and to evaluate the effect of the resultant enhanced dissipation on the jet. The details of the study configuration are summarized in section 2 (more detail is given by *Perlin et al.* [2005a]). A discussion of the observations appears in section 3; in particular, the characteristics of the midwater turbulence and shear. Shear data were obtained from both shipboard acoustic Doppler current profiler (ADCP) and three mooring records, providing two quite different perspectives. In section 4 we consider how the enhanced turbulence affects the jet dynamically and how it affects mixing in the coastal ocean. A summary and conclusions are presented in section 5.

2. Instrumentation and Study Configuration

[7] Data discussed in this study were obtained off the Oregon coast during the spring of 2001 as part of the Coastal Ocean Advances in Shelf Transport (COAST) experiment (Figure 1) [*Barth and Wheeler*, 2005]. Shipboard data were collected from R/V *Thomas G. Thompson*, from 19 to 28 May 2001 along 12 successive cross-shelf transects at approximately 45°N. Transects are labeled in hours from the beginning of the first transect, and cross-shelf distance is shown in kilometers, following the convention used in earlier papers [*Perlin et al.*, 2005a]. Transects ranged from inside of the 40-m isobath to the 250-m isobath, for a total length of ~25 km. Vectors have been decomposed into cross-shelf (**x**) and along-shelf (**y**) vectors with positive values indicating shoreward and northward, respectively. Along-shelf and cross-shelf directions are oriented along the local shelf axis (for which the $+y$ direction has been rotated 7° clockwise from true north).

[8] Shipboard data include velocity profiles obtained with a 150-kHz ADCP sampled once every 6 s with 4-m depth bins averaged into 3-min blocks. Vertical profiles were made continuously with our loosely tethered microstructure profiler, Chameleon, equipped with sensors to measure pressure, acceleration, temperature, conductivity, turbidity (880-nm backscatter), and microstructure shear, from which the turbulence dissipation rate ε was computed [*Moum et al.*, 1995]. The profiler fell at ~1 m s^{-1}, yielding profiles every 1–5 min, depending upon water depth. Chameleon was fitted with a bottom crasher ring which allowed the

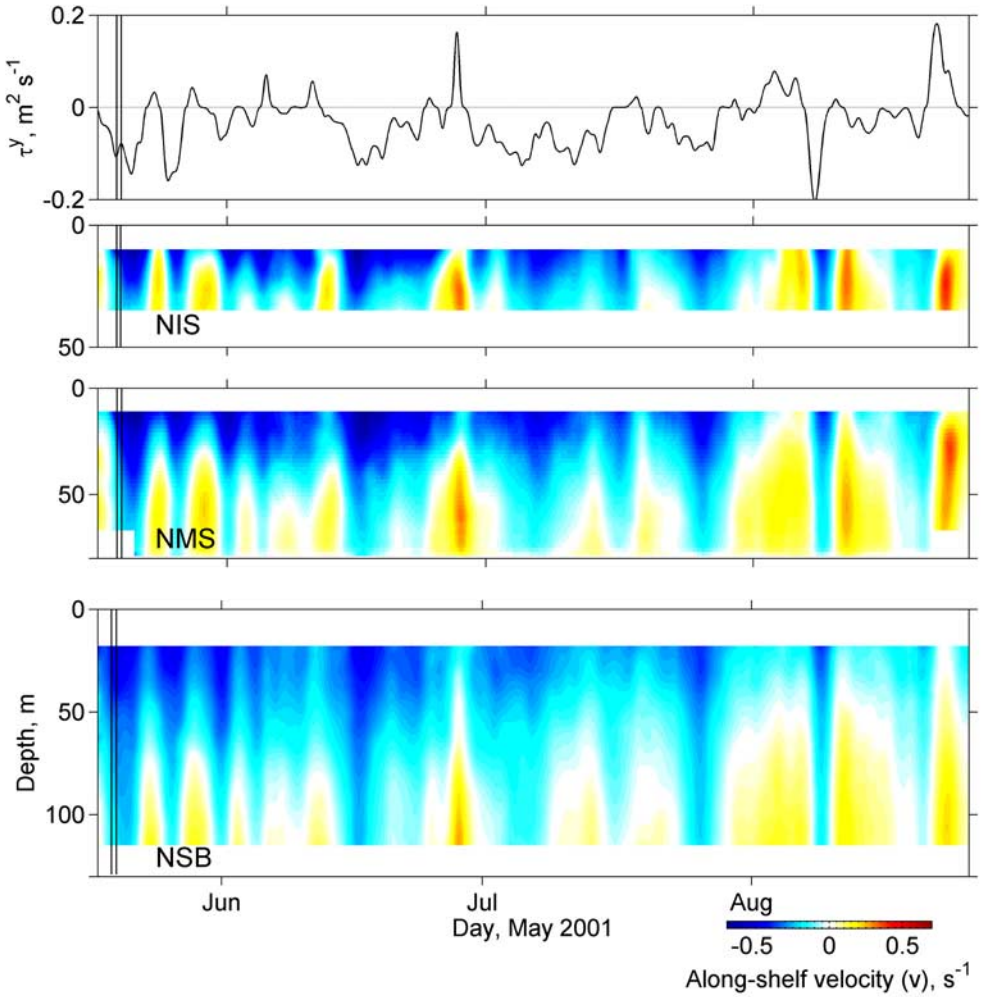

Figure 2. (top) Along-shore wind stress (northward positive) derived from 36-hour low-pass-filtered wind stress. (bottom) The 36-hour low-pass-filtered along-shelf velocities v from moorings NIS, NMS, and NSB. Data from the entire mooring deployment are shown. The 9-day period during which ship observations were taken along the mooring array is marked as the region between the two vertical lines.

instrument to be run directly into the bottom, yielding measurements to 2 cm above bottom. The noise floor of ε is approximately 10^{-9} m^2 s^{-3} with the nose crasher ring configuration employed here.

[9] Three moorings were deployed along the transect line (45°N) during an overlapping three month period, 15 May to 27 August, 2001 [*Boyd et al.*, 2002]. The moorings were located at north shelf break (NSB), north midshelf (NMS), and north inner shelf (NIS) in water depths of 130, 81, and 50 m, respectively. A meteorological buoy was colocated with the midshelf mooring. The moorings were instrumented with a number of T and C sensors as well as acoustic Doppler profilers. The NSB mooring was equipped with a SonTek 250 kHz acoustic Doppler profiler (ADP) sampling 4-m bins set 6 m above bottom, while the NIS mooring was equipped with a RDI 300-kHz ADCP sampling 2-m bins set 4 m above the bottom. The NMS mooring was equipped with two Doppler profilers: a RDI 300 kHz ADCP sampling 2-m bins set 4 m above the bottom and a 1 MHz Aquadopp current profiler placed 10 m above the bottom (looking downward) sampling 1/2-m bins, to capture the near-bottom flow. The placement of sensors and further details are given by *Boyd et al.* [2002].

3. Observations

3.1. Moored Observations of Velocity and Shear

[10] Previous observations of Oregon's upwelling show that along-shelf depth-averaged velocity responds quickly (within a few hours) to changes in along-shelf wind [e.g., *Huyer et al.*, 1972]. There exists a strong correspondence between the reversals of the depth-averaged velocity measured at each of the moorings with wind relaxation/reversal events, with little lag [*Barth et al.*, 2005]; a response that is reflected in this data set (Figure 2). A subset of the mooring record which coincides with our observation period (Figures 3a and 3b) shows two wind relaxation events; the ocean's response is clearly seen in the along-shelf velocities (Figure 3b). One relaxation event occurred from

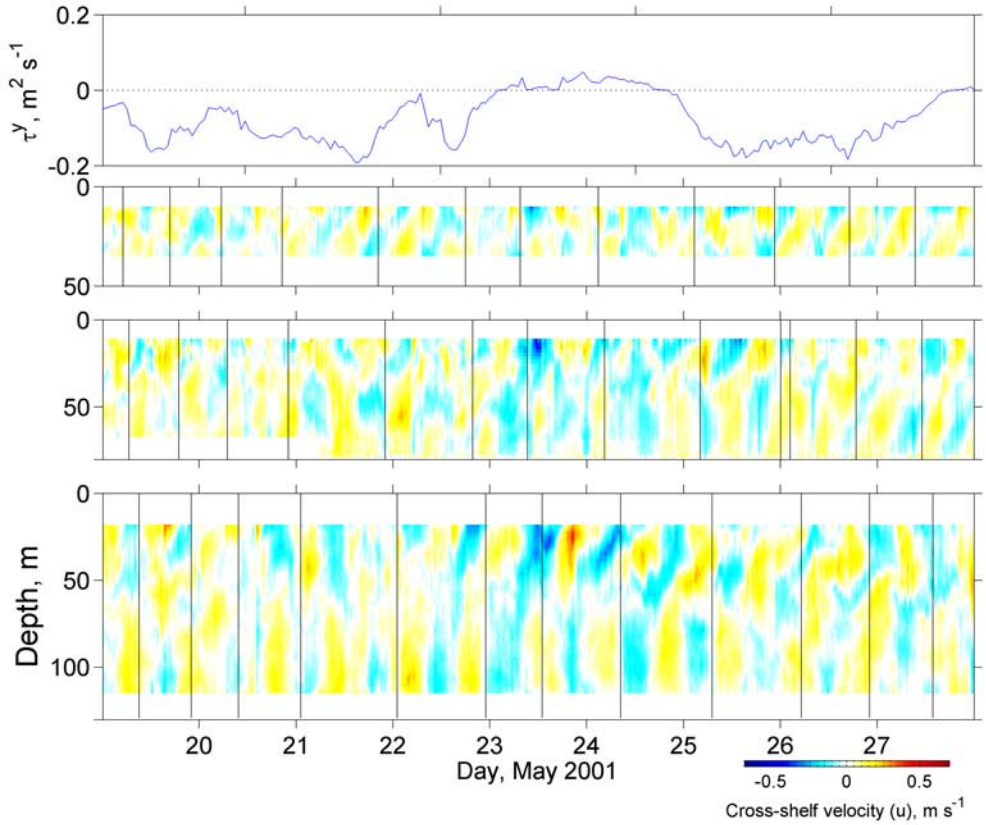

Figure 3a. (top) Along-shelf wind stress (northward positive). (bottom) Cross-shelf velocity u from moorings NIS, NMS, and NSB during the same time period as the ship measurements. Vertical black lines indicate times at which the ship crossed the cross-shelf position of the mooring. Velocities were low-pass filtered with a 1-hour cutoff.

23 to 25 May, coincident with transects +85 hours through +142 hours. The second relaxation event had just begun at the end of the 9-day study period, coincident with transect +197 hours.

[11] In addition to the slow variation seen in Figure 2, the data record also includes higher-frequency variability; the cross-shelf signal is dominated by narrowband (in frequency) oscillations with a period of the order of 10 hours: we will demonstrate subsequently that these oscillations are primarily the signature of M_2 and near-f IGWs (Figure 3a). These higher-frequency oscillations are present in the along-shelf velocity (Figure 3b) along with a strong barotropic and baroclinic low-frequency velocity signal associated with the upwelling jet. The maximum velocities in the coastal jet observed during this study period are $\sim$0.7 m s^{-1}. In comparison, higher-frequency velocity fluctuations have magnitudes of $\sim$0.2 m s^{-1}.

[12] Unlike the along-shelf velocity, the response of along-shelf shear to wind relaxation/reversal events is weak. While the depth-averaged velocity includes many reversals of direction (Figure 2), the 36-hour low-pass filtered along-shelf shear is positive for the entire 3-month record (Figure 4). This insulation of subinertial along-shelf shear to wind relaxation events was first described by *Huyer et al.* [1979], who noted that the upwelled isopycnal structure and associated shear vary over timescales of weeks. The subinertial shear weakened over the duration of the mooring deployment, from a typical maximum value of $\sim$0.01 s^{-1} at the base of the upwelling jet (e.g., NMS, 40-m depth) to approximately half that value 2 months later (Figure 4).

[13] Higher-frequency shear is apparent in the shorter 1-hour low-pass-filtered record (Figures 5a and 5b). This is associated with IGWs of primarily near-f and M_2 frequency (Figure 6). These records highlight the fact that the dominant shear contributions arise from two sources widely separated in frequency, the IGW field with a timescale of O(10) hours and the thermal wind shear of O(10) days. Therefore we employ a construct based upon a three-term decomposition of the flow based on these two timescales and that of the turbulence. We describe the shear field as

$$\boldsymbol{S} = \boldsymbol{S}_0 + \widetilde{\boldsymbol{S}} + \boldsymbol{s}', \tag{1}$$

where the $\boldsymbol{S} = [\partial u/\partial z, \partial v/\partial z]$ has been decomposed into three components: a microstructure component $\boldsymbol{s}'$, which represents the shear on turbulence timescales; a wave component $\tilde{\boldsymbol{S}}$, which represents shear associated with the IGW field; and a "low-frequency" component $\boldsymbol{S}_0$, which represents the field at subinertial frequencies. (Although equation (1) explicitly describes the decomposition in shear, this timescale decomposition is used generally for all variables in this study.) The microstructure component $\boldsymbol{s}'$, while measured via the shear sensors on Chameleon, is not discussed directly; instead, we use those data to calculate ε.

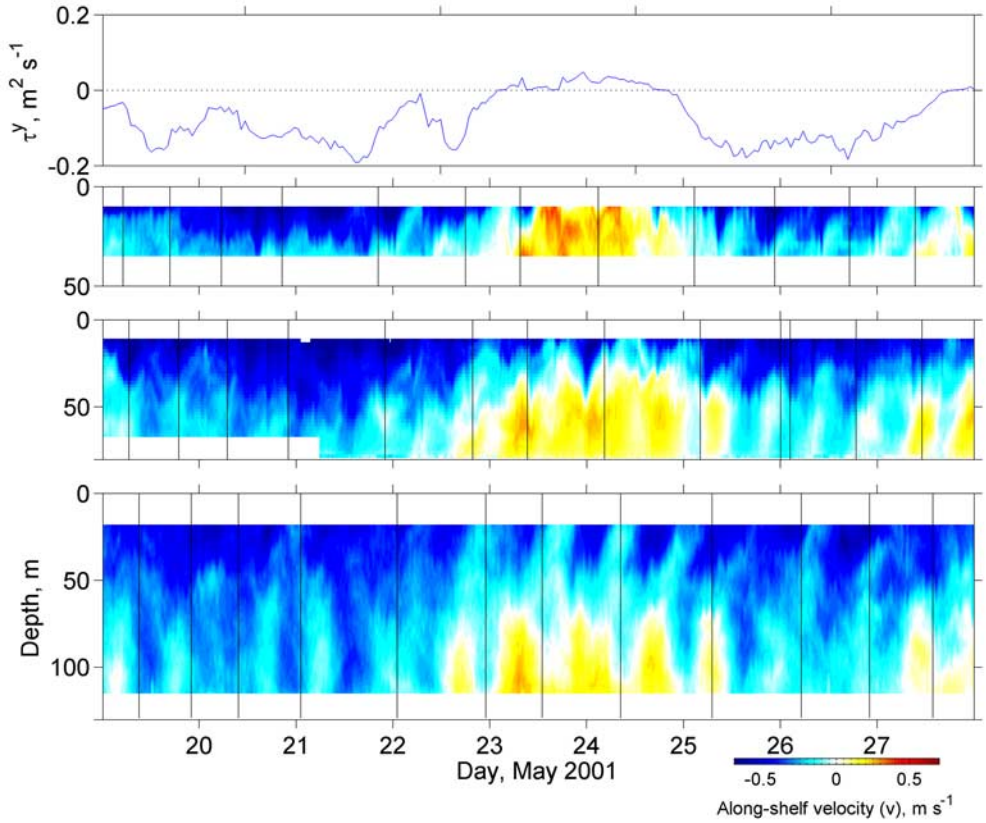

Figure 3b. (top) Along-shelf wind stress (northward positive). (bottom) Along-shelf velocity v from moorings NIS, NMS, and NSB during the same time period as the ship measurements. Vertical black lines indicate times at which the ship crossed the cross-shelf position of the mooring. Velocities were low-pass filtered with a 1-hour cutoff.

[14] The low-frequency component $\boldsymbol{S}_0$ is defined as the mean value of $\boldsymbol{S}$ calculated over the duration of the 9-day experiment. (This is necessitated by the fact that the data collected via the ship transects do not resolve variability over timescales of O(10) days.) Quantities measured from mooring data will be denoted by the identifier "M," while those measured from shipboard measurements will be denoted by "S." Thus the low-frequency thermal wind shear evaluated at a mooring ${}^{M}\boldsymbol{S}_0$, is simply the 9-day mean as a function of depth. We discuss the method by which we estimate the low-frequency thermal wind shear from the ship transects ${}^{S}\boldsymbol{S}_0$ in section 3.2.

[15] The wave component of shear $\tilde{\boldsymbol{S}}$ includes internal wave shear spread over a wide frequency band. Spectra of shear computed using 10-day record lengths with 5-day overlap exhibit dominant peaks at near-f and M_2 frequencies (Figure 6). The magnitude of the M_2 shear variance is largest at the inshore mooring. There is an order of magnitude decrease in M_2 shear variance between that observed at the inner mooring and that observed at the outer mooring. In contrast, near-f shear variance is comparable at all three moorings. The middle mooring shear contains approximately equal shear variance between the near-f and M_2 bands.

[16] Maximum values of the IGW shear are about twice that of the shear associated with the thermal wind. (Maximum amplitude of $\tilde{\boldsymbol{S}}$ over the 9-day study period is $\sim 0.02\ s^{-1}$, as shown in Figure 5a. This value ($\sim 0.02\ s^{-1}$) is the 2σ value during this period. Maximum values of $\boldsymbol{S}_0$ are found at the base of the upwelling jet, with values of $\sim 0.01\ s^{-1}$, as shown in Figure 4, third panel.) The largest values of S^2 occur when $\boldsymbol{S}_0$ and $\tilde{\boldsymbol{S}}$ interfere constructively, producing values of $S^2 \sim 10^{-3}\ s^{-2}$, 10 times greater than that from the thermal wind shear and ~ 2.5 times greater than that from the internal wave shear alone. We quantify the contribution of $\boldsymbol{S}_0$ to $\boldsymbol{S}$ via histograms (Figure 7). At each mooring and for the ship data (see section 3.2) the thermal wind shear is broken into two subsets: one which includes the smallest 25% of $\boldsymbol{S}_0$ data, the other which includes the largest 25% of $\boldsymbol{S}_0$ data.

[17] Histograms are computed for both the IGW shear and the total shear based upon these two subsets; the distributions are nearly identical for the low thermal wind shear subset of the data (and thus the mean values of the two distributions are approximately equal). In contrast, both the mean and maximum values of $\boldsymbol{S}$ are considerably larger than $\tilde{\boldsymbol{S}}$ alone for the high thermal wind shear subset, except in the case of the data taken at NSB. For this location, all four histograms are nearly identical; the reason being that the thermal wind shear at this distance offshore is very weak; consequently, $\tilde{\boldsymbol{S}}$ is the dominant contributor to $\boldsymbol{S}$. The histograms produced from the ship data are, in effect a weighted average of the shear distributions of all three moorings.

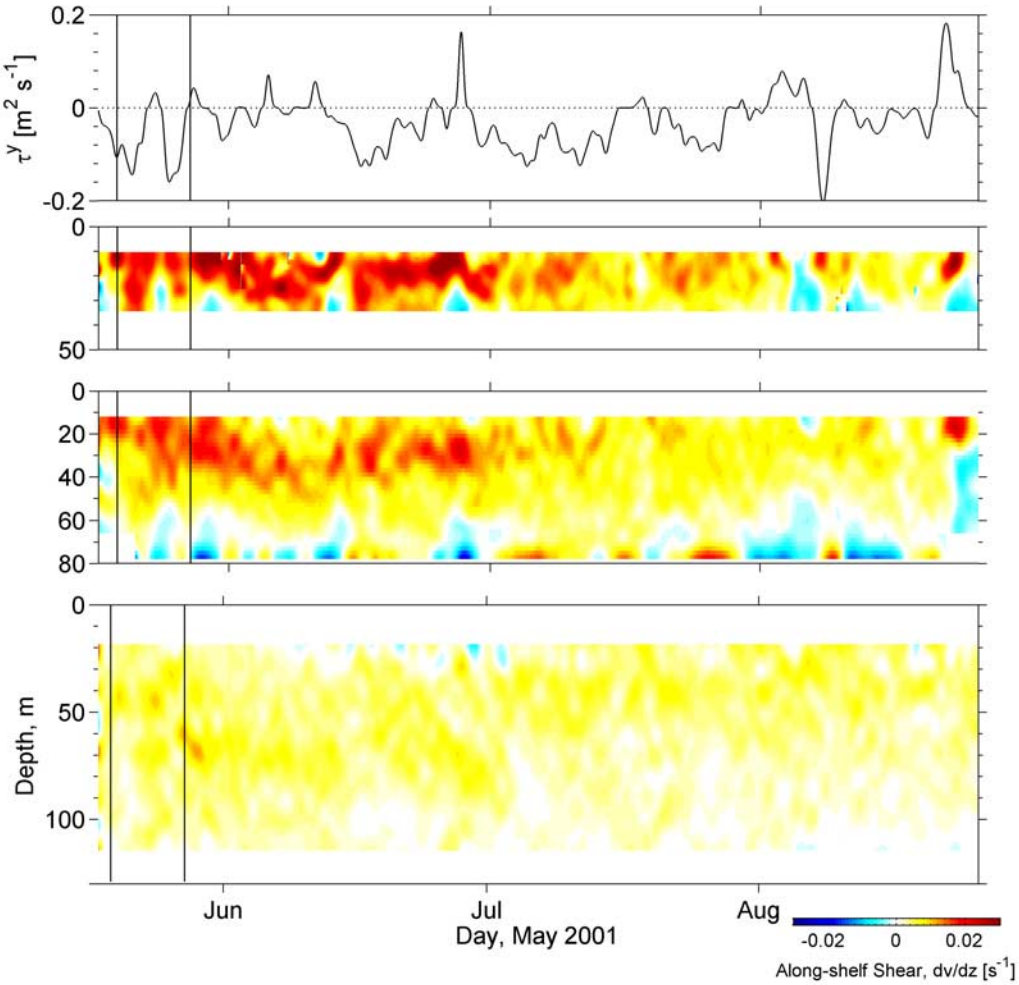

Figure 4. (top) Along-shelf wind stress (northward positive) derived from 36-hour low-pass- filtered wind stress. (bottom) The 36-hour low-pass-filtered along-shelf shear *dv/dz* from moorings NIS, NMS, and NSB. Data from the entire mooring deployment are shown. The 9-day period during which ship observations were taken along the mooring array is marked as the region between the two vertical lines.

[18] Also note that the mean value of $\tilde{\boldsymbol{S}}$ is larger for the large thermal wind subset compared to the small thermal wind subset (or $\tilde{\boldsymbol{S}}$ tends to be larger when $\boldsymbol{S}_0$ is large) at moorings NIS and NMS. It is possible that this is associated with the density structure, in that when the isopycnals are packed closely together (e.g., near the surface), both the buoyancy frequency and the baroclinic pressure gradient will be larger than at locations where the isopycnals are well separated. Thermal wind shear and the IGW shear will both be larger in regions of increased horizontal density gradient and vertical density gradients. This has the important consequence that larger values of both thermal wind and IGW shear are found at the base of the upwelling jet.

[19] It is also possible that nonlinear transfer of energy between $\tilde{\boldsymbol{S}}$ and $\boldsymbol{S}_0$ occurs. In order to ascertain if there is some further interaction between $\tilde{\boldsymbol{S}}$ and $\boldsymbol{S}_0$, one must isolate the influence of the density gradient, perhaps via the use of WKB-scaled coordinates. Unfortunately, this analysis was not possible with the current data set.

[20] Although both near-*f* and M_2 shear are first-order contributors to $\tilde{\boldsymbol{S}}$, the cross-shelf structure of $\tilde{\boldsymbol{S}}$ is not uniform; their contributions vary across the shelf. The magnitude of $\tilde{\boldsymbol{S}}$ tends to increase toward the shore, a trend that is visible in Figures 5a and 5b. Additionally, the near-*f* and M_2 shear magnitudes vary differently with cross-shelf distance. Near-*f* shear variance decreases slightly offshore, in contrast to M_2 variance which decreases by over an order of magnitude (Figure 6) over the same distance. Using a coastal WKB scaling [*Levine*, 2002] to stretch the vertical coordinate and thus weight the shear with respect to the local buoyancy frequency, we find that the depth-integrated near-*f* shear variance is constant, while the depth-integrated M_2 shear variance decreases significantly offshore (Figure 6 inset). As a result, the observed internal wave shear shifts from primarily near-inertial offshore to primarily M_2 onshore; in addition, the total shear variance increases toward the coast.

3.2. Shipboard Observations of Velocity and Shear

[21] The shipboard observations are temporally aliased as an individual transect was completed in approximately 9 hours, close to an M_2 tidal period. Because the internal wave field contains spatial variability (cross-shelf positional

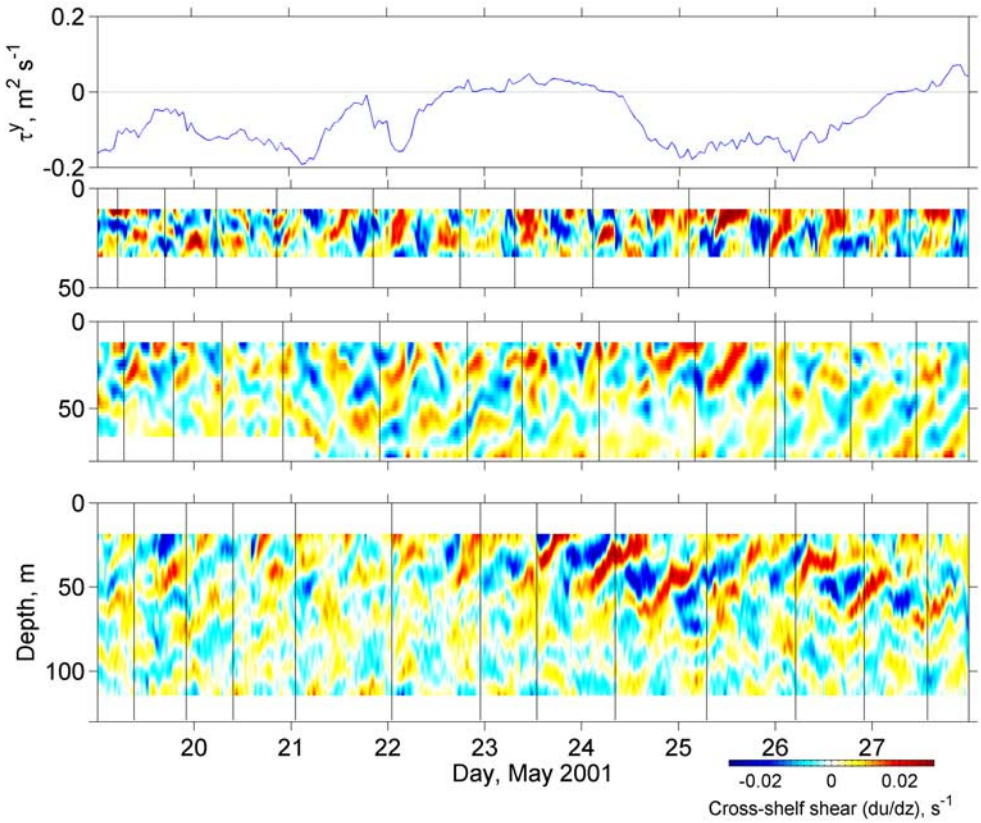

Figure 5a. Cross-shelf shear *du*/*dz* from moorings (top) NIS, (middle) NMS, and (bottom) NSB during the same time period as the ship measurements. Vertical black lines indicate times at which a ship transect passed the mooring in question. Data were temporally filtered with a 1-hour low-pass cutoff Butterworth filter. The measured along-shelf wind stress is shown above the shear measurements.

dependence, in both phase and amplitude), identification of frequency components from ship's ADCP is more difficult than from velocities obtained from fixed moorings.

[22] While a clear signature of the internal wave field is difficult to discern in shipboard-derived shear measurements (Figures 8a and 8b), the data do contain features consistent with those observed in the moored data (Figures 5a and 5b). Thin layers of shear with multiple reversals are seen in the transect data, sometimes as coherent cross-shelf structures, for example, three bands in transect +181 hours stretching from x = 5 km to x = 22 km. As in the mooring data, the depth-averaged cross-shelf shear is nearly zero, while the along-shelf shear ${}^{S}S^{y}$ is offset to positive values because of the presence of the low-frequency thermal wind shear.

[23] To separate the internal wave shear from thermal wind shear in the transect data, we employ a phase-weighted average (PWA). The entire 9-day transect shear record is binned by cross-shelf position (bin width 400 m) and depth. Each bin is sparsely populated temporally by 12 clusters of data each corresponding to one of the 12 cross-shelf transects, separated over the 9-day sampling period (with a mean temporal separation of ~19 hours). Fortunately, this sampling period is not phase locked to either the near-f or M_2 frequency bands.

[24] While an arithmetic mean will partially separate $\boldsymbol{S}_0$ and $\widetilde{\boldsymbol{S}}$, portions of the phase space are oversampled while other portions are undersampled, leading to cross-talk between the two signals. To mitigate this, we weight each measurement by its position in phase space, such that all phases are equally weighted for one frequency: We choose our weightings such that the M_2 frequency is equally represented in phase. While potentially better than a simple unweighted average of all data, the PWA has a drawback in that only one frequency can be weighted properly. Because our data have significant (and nearly equal) internal wave shear variance at both M_2 and near f, the averaging is not optimum for a significant portion of the shear signal. The M_2 frequency was chosen as the weighting frequency because M_2 variance is relatively narrowband compared to near-f variance, the weighted average will have the most impact on the narrowband signal. Additionally, implementing the PWA on the M_2 frequency band extracts the low-frequency signal most cleanly near the coast, where both the M_2 shear variance and the shear associated with the upwelling jet are largest.

[25] The accuracy of the PWA technique in extracting $\boldsymbol{S}_0$ (Figure 9b) from ${}^{S}\boldsymbol{S}$ is evaluated in two ways. First, we compare the thermal wind shear computed directly from the PWA density field (denoted ${}^{T}\boldsymbol{S}_0$, Figure 9c). The two estimates are similar, both in magnitude and structure. The correspondence between these two fields suggests that we have done a reasonable job in both removing the higher-frequency internal wave field from the data and in isolating

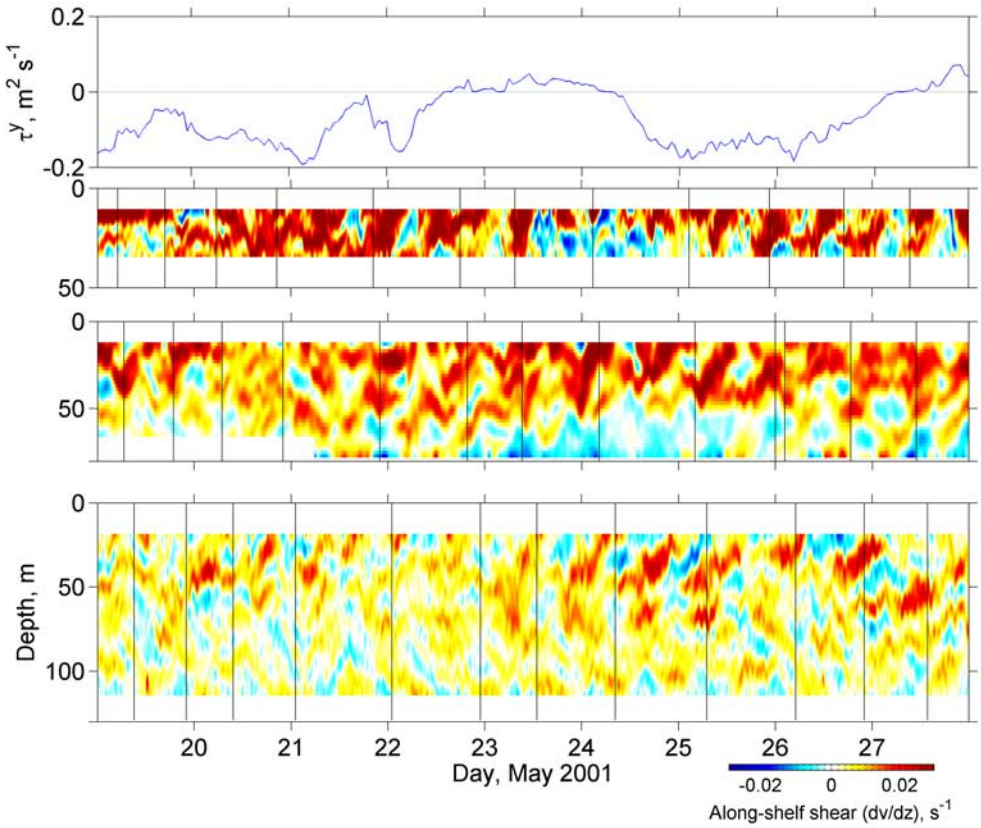

Figure 5b. Along-shelf shear *dv*/*dz* from moorings (top) NIS, (middle) NMS, and (bottom) NSB during the same time period as the ship measurements. Vertical black lines indicate times at which a ship transect passed the mooring in question. Data were temporally filtered with a 1-hour low-pass cutoff Butterworth filter. Shown above the shear measurements is the measured along-shelf wind stress.

the thermal wind shear in the velocity measurements, as internal wave perturbations to the density and velocity structure would not be geostrophic. Second, we compare these two shear estimates ${}^{T}\boldsymbol{S}_0$ and ${}^{S}\boldsymbol{S}_0$ with ${}^{M}\boldsymbol{S}_0$, computed directly from the mooring data (Figure 9a, the locations of each mooring are denoted as vertical lines). Both estimates of along-shelf low-frequency shear are in good agreement in magnitude and depth dependence when compared to the mooring data. The region of maximum low-frequency shear is contained between the ~100-m isobath inshore to the ~40-m isobath, occupying a width of ~10 km. Offshore of this core, there exists a weak thermal wind shear, decreasing to near-zero approximately 10 km farther offshore. The implementation of our PWA technique on the shear signal produced encouraging results, and on the basis of this we extend its use in section 4.

[26] As with the mooring data, shipboard data demonstrate that maximum $|\boldsymbol{S}|$ occurs when both $\boldsymbol{S}_0$ and $\tilde{\boldsymbol{S}}$ are large (Figure 7, bottom). We note that the character of the histograms computed from the shipboard data is highly weighted toward data such as that found at NSB because of the fact that ~3/4 of the total data per transect (in area) were obtained offshore of the 100-m isobath. Additionally, we note that all values of shear obtained from the ship are smaller in magnitude than that observed at the moorings: This is a consequence of the larger bin size on the shipboard ADCP along with the necessary spatial averaging in that data set to reduce the noise.

3.3. Shipboard Observations of ε

[27] Observed values of ε vary by 5 orders of magnitude, from 10^{-9} to 10^{-4} W kg^{-1} (Figure 10). The largest values were found in the surface mixed layer and bottom boundary layer and are discussed elsewhere [e.g., *Perlin et al.*, 2005a]; here we focus on the midwater column turbulence. The physical extent of the boundary layers was determined by identifying surface and bottom regions for which the observed dissipation was at least 10^{-8} W kg^{-1} continuously from the boundary. In practice, however, the region of the water column for which there was no ADCP data was always larger than the layers so defined. (Sidelobe reflection and the near-ADCP blanking region prevent measurements of near-bottom and near-surface velocity, respectively.) We therefore avoid including data from either the surface or bottom boundary layer by including only data within the ADCP depth range where there are simultaneous measurements of turbulence, large-scale velocity and shear, and density (through T and S).

[28] Away from boundaries, values of ε range from 10^{-9} to 10^{-6} W kg^{-1}. Small values of ε make up the majority of observations within the midwater column and are associated with the noise floor of the instrument. Visual inspection of these data indicates that values above the noise floor are

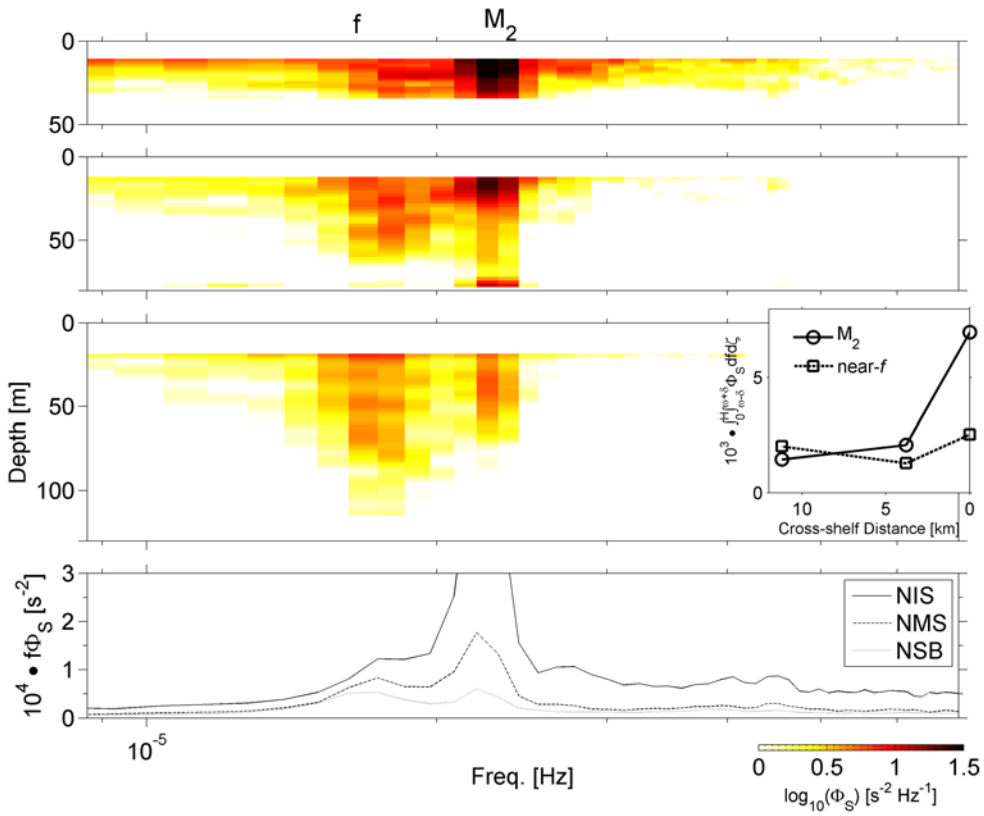

Figure 6. Magnitude of the shear spectra computed for each mooring as a function of frequency and depth. (top) Log of the power spectral intensity for each of the three moorings as a function of depth. (bottom) Vertically averaged spectral intensity for each mooring plotted in variance preserving form (the M_2 peak of mooring NIS has a peak value of 6×10^{-4} s^{-2}). Also shown is the location of the inertial frequency f and the semidiurnal frequency M_2. Shown in inset is the vertically integrated (in stretched coordinates) shear variance in the M_2 (solid line with circle) and near-f (dotted line with square) bands for each mooring. The shear variance of the near-f band and the M_2 band is estimated by integrating the frequency spectrum over periods 13.5–18 hours and 11.3–13.5 hours, respectively.

primarily found in thin (∼10 m thick) but horizontally coherent (∼1–10 km) bands of elevated dissipation observed in all transects (Figure 10). These "sheets" of active turbulence have horizontal to vertical aspect ratios of order of 100–1000. The word sheets, rather than "filaments," is chosen because we assume some three dimensionality to the observed layers of high σ; this three dimensionality is not observed directly but can be inferred by the fact that these structures are coherent over both many kilometers of across-shelf distance but also over many hours required to complete the transect as the flow is being advected past the ship (via the along-shelf jet). One example of such a feature is apparent in transect +197 hours, which contains two sheets separated by ∼30 m, each of which extend offshore nearly 15 km. We will demonstrate that this structure in dissipation is related to the structure of the shear; in particular, it is associated with regions in which constructive interference between the internal wave shear and the background shear produces very large values of S^2.

[29] The inverse Richardson number, $Ri^{-1} = S^2/N^2$, was computed for the thermal wind shear alone, internal wave shear alone, and the total shear field (Figure 11, one transect shown, other transects are similar). Ri^{-1} was chosen to aid visual comparison between regions unstable to shear instabilities (large Ri^{-1}) and elevated ε. Most striking is the clear correspondence of ε with regions of large IGW-derived Ri^{-1}, both of which take the form of long, thin patches. In contrast, the shear associated with the thermal wind field is weak and insufficient to elevate Ri^{-1} to near-critical values: The geostrophically adjusted jet, in the absence of the IGW field, would be unable to generate regions unstable to shear instability. Nevertheless, the thermal wind shear contributes to the elevated S^2 via superposition. Values of Ri^{-1} inside the 100-m isobath are generally higher than values outside (Figure 10), a result of the $\boldsymbol{S}_0$ contribution to the total shear.

[30] The intermittent nature of the dissipation signal makes objective determination of a sheet of elevated ε difficult. Instead, we identify regions of large inverse Richardson number ($Ri^{-1} > 1$). We refer to data falling within these regions as masked data; this mask has been contoured onto the dissipation map in white (Figure 11, bottom). The patches delineated by the mask are typically long (∼1–10 km) and thin (∼10 m) and clearly contain much of the observed elevated dissipation. Normalized histograms of $\log_{10}(\varepsilon)$ for the entire data set, data within the Ri mask, and data outside of the mask were computed

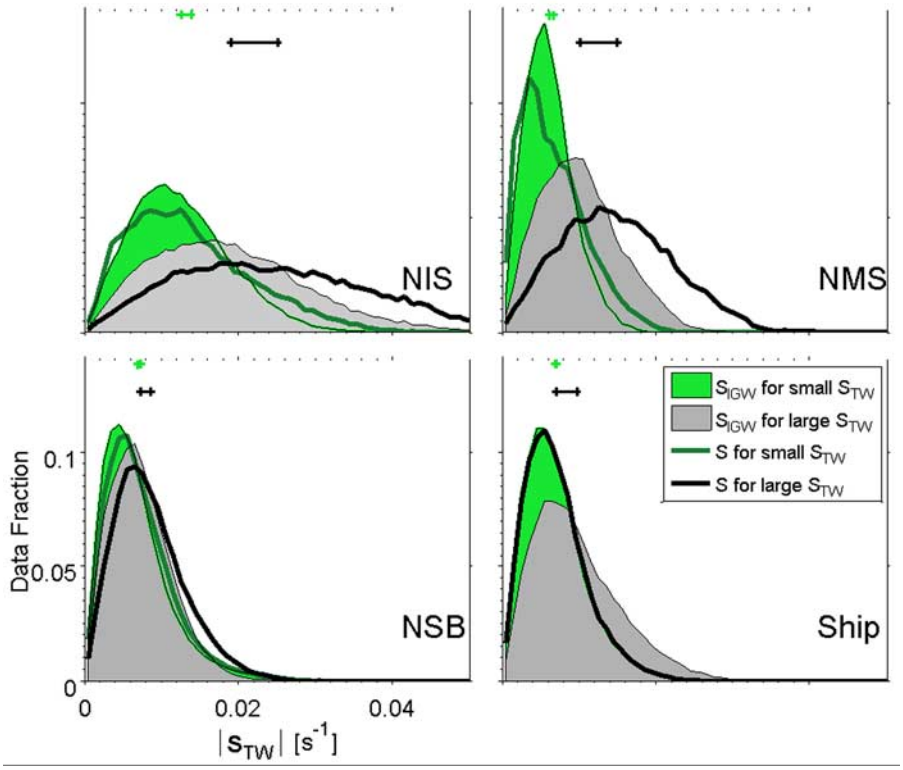

Figure 7. Histograms of shear data for mooring and ship data sets. In each case the total shear has been decomposed into thermal wind and internal gravity wave components. Data have been partitioned into two subsets, each of which is composed of 25% of the total data: One subset includes the minimum values of thermal wind shear (green), and the second includes the maximum values of thermal wind shear (black). Histograms of internal gravity wave shear (shaded areas), and total shear (solid lines). The mean value of each histogram is shown on the top (marked with a cross). Each line indicates the difference between the means of the internal gravity wave shear and the total shear (low thermal wind subset (green) and high thermal wind subset (black)). Note that both the shapes and the statistics associated with the IGW and total shear are nearly identical for the low thermal wind subset, while the total shear is significantly elevated for the large thermal wind subset. This is the affect of the superposition of the thermal wind shear with the IGW shear on the total shear field.

(Figure 12a). Mean values of ε for each histogram demonstrate that the masked data contain a much higher-percentage of large ε; there is a factor of 5 difference in ε between data falling within and data falling outside the masked regions. Because of the low occurrence of high-ε events relative to low-ε events we include a second metric to ascertain the usefulness of the masks in isolating high-ε events: the cumulative distribution function (Figure 12b). We find that $\sim$65% of the "large" ε data ($\varepsilon > 3 \times 10^{-8}$ W kg^{-1}) is included in the masked regions, while only $\sim$15% of "small" ε data ($\varepsilon < 3 \times 10^{-9}$ W kg^{-1}) falls inside the mask. The percent of total area falling inside the mask is slightly less than 14% of the total cross-sectional area shown.

[31] We define contiguous regions within the *Ri* mask and refer to each as a "patch." Patch statistics provide a quantitative description of the "shape" of the turbulence sheets identified by the mask. Note that the patches, in general, underestimate the cross-shelf length of mixing sheets because a small gap in the masked region will delineate two separate patches in the calculation. The horizontal resolution of the data is based upon the spatial distance between Chameleon profiles ($\sim$150 m). The vertical resolution of the data is based upon the vertical spacing of Chameleon data and ADCP bins. Although the data have been mapped onto 1-m vertical bins for dissipation and conductivity-temperature-depth (CTD) data, the resolution of the ADCP data (and therefore the patches) is $\sim$4 m in the vertical. Patches included within these calculations were required to include at least 25 contiguous data points, effectively eliminating the effect of very small patches. An obvious concern is that the aspect ratio of the sampling may weight the observed aspect ratio simply because the vertical resolution is so much finer than the horizontal resolution. However, the aspect ratio associated with the measurements in the mask is $\sim$40 ($\sim$150 m horizontal, cast to cast distance, and $\sim$4 m vertical, bin size of ADCP), a value well below the peak of the distribution. This results in a total of 157 patches.

[32] Histograms of patch width and patch height are shown in Figure 12c. The distribution of patch height shows a strong preference for patches with 5–15 m thickness: The largest patch height in the record is 30 m. In contrast, the patch width histogram does not have a similar unimodal

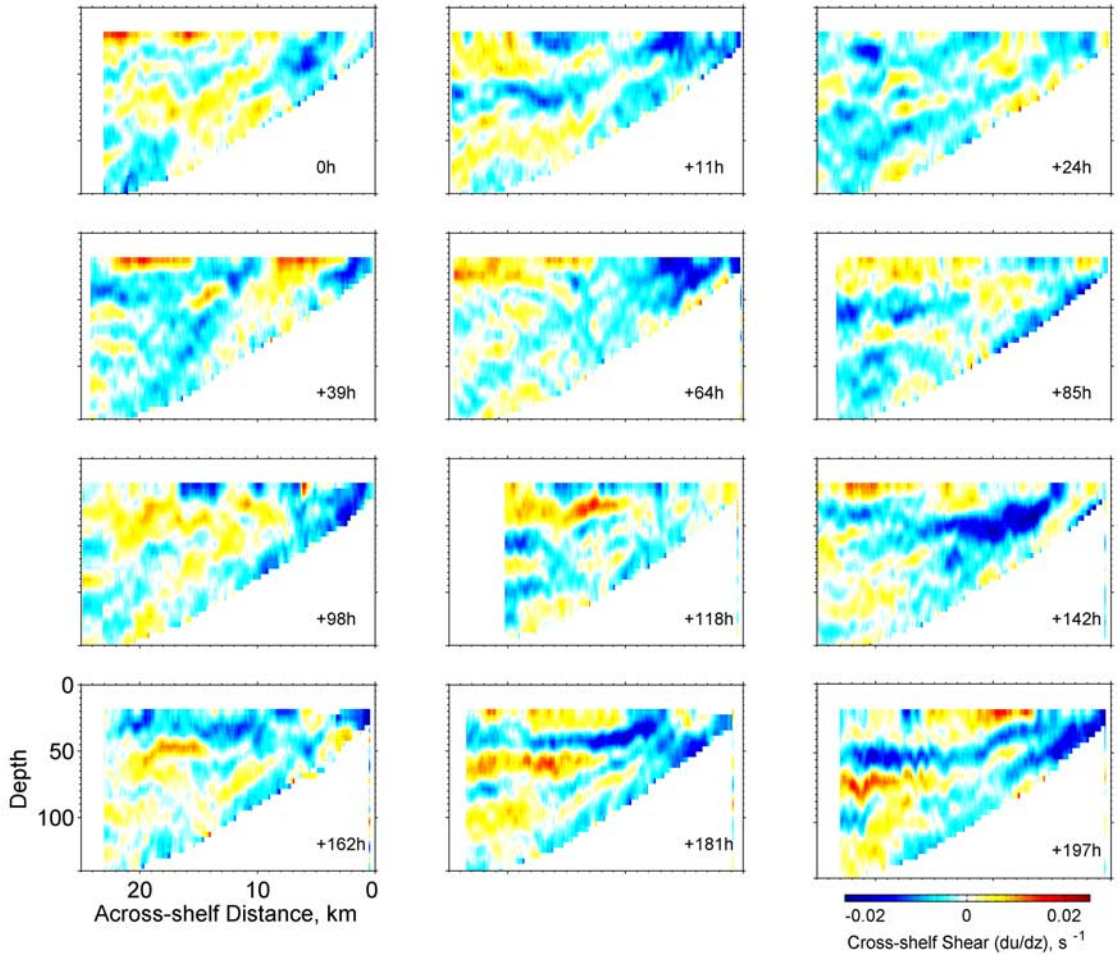

Figure 8a. Cross-shelf shear *du*/*dz* sections for each of the 12 transects conducted. The first transect is shown at the top left, moving sequentially to the right and down.

distribution. There are a large number of observed patches between 1 and 5 km in length, but there is a second peak in the distribution indicating a large number of ~25-km patches (patches that span the entire width of the cross-shelf transect). These very long patches correspond to the sheets of high-ε described previously qualitatively, such as that shown in the example cross section of Figure 10. Patch aspect ratio (path length divided by patch height) is characterized by a histogram that shows a broad peak corresponding to aspect ratios between 100 and 1000, with a maximum at 400 (Figure 11). Another concern is the proper way to measure patch width and height, given the large anisotropy of the patch dimensions and the fact that the patches often slope. Consequently, we define patch width as the maximum horizontal distance between all the contiguous points defining a single patch. In contrast, patch height is defined as the mean top-to-bottom separation of the patch across its entire extent.

4. Discussion

[33] The preceding analysis demonstrates that regions of high Ri^{-1} (formed by the superposition of the IGW field with the background thermal wind shear) coincide with regions of high ε. We expect that this is dependent upon the specifics of the flow: the topography of the shelf, the internal wave field propagating upon it, and the specific form of the low-frequency shear component, all of which may vary from region to region. Thus it is possible that there is an along-shelf spatial dependence that we cannot address here. However, we submit that the coincidence of a linear IGW field with geostrophically driven jets and coastal currents must be common in the coastal environment and therefore the elevated dissipation observed here should also be common.

[34] Midwater turbulence generation in this data set requires the IGW field to provide the necessary shear. Another source of critical shear requiring an IGW field (resulting in midwater turbulence generation) was discussed by *MacKinnon and Gregg* [2003a, 2003b, 2005a, 2005b] wherein coastal midwater turbulence (somewhat weaker than described here, although still significantly above background levels) was hypothesized to be driven via transfer of energy through the IGW field to small scales. Thus the presence of a linear IGW field appears to be a critical component in the generation of coastal turbulence and mixing. *Winkel et al.* [2002] also found larger values of dissipation corresponding to region in which IGW shear was superimposed upon a low-frequency current shear (in their case, this occurred in the Florida Current; unfortunately,

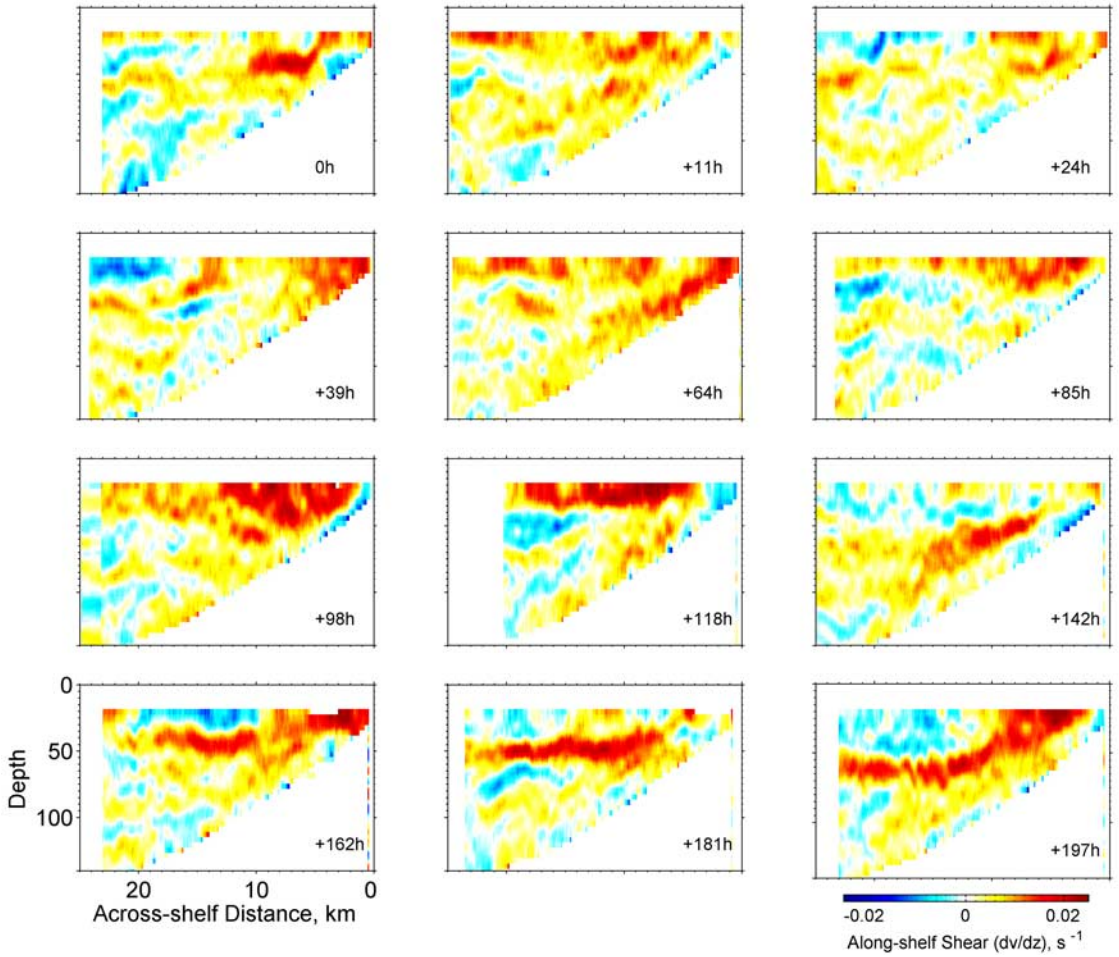

Figure 8b. Along-shelf shear *dv*/*dz* sections for each of the 12 transects conducted. The first transect is shown at the top left, moving sequentially to the right and down.

their data were such that they were unable to decompose the IGW shear to determine if it was a Garrett Munk (GM)-like field or a narrowband wave field such as that observed here).

[35] Unfortunately, oceanographic studies often ignore the dynamical impact of the internal wave field in experimental and modeling studies of the coastal ocean. This is particularly troubling in numerical models which employ a turbulence closure scheme (be it Mellor-Yamada, k-ε, etc.) requiring knowledge of local N^2 and S^2. For models to properly account for mixing, either the model must include a realistic internal wave field (so as to properly drive the closure scheme) or an improved parameterization must be included to account for these processes. As the shear associated with the geostrophic flow is typically weak compared to the stratification, turbulence viscosity in the model will default to a "background" value within the core of such currents [*Garvine*, 1999] in the absence of a secondary shear source. This effect can be seen in a direct comparison between the observed flow field for the first of the 12 transects and a model simulation of that same flow field [*Kurapov et al.*, 2005]. This model, as is the case with nearly all coastal models, did not include a IGW field (either M_2 or near f) and therefore produces a midwater column devoid of turbulence (and mixing) above background values.

4.1. Role of the Turbulent Stress Divergence in Jet Deceleration

[36] Having discussed the observations of elevated midwater turbulence, we now discuss the effect this turbulence has on the background flow. To do so, we again turn to the PWA technique in order to calculate estimates of average turbulence quantities over timescales of the geostrophic flow's variability ("low-frequency" timescales with respect to equation (1)). In order to ascertain the role of the enhanced turbulence on the geostrophic flow field we estimate an eddy viscosity and subsequently a turbulence stress. As discussed previously (equation (1)), we employ a three-scale decomposition to derive these quantities [e.g., *Anis and Moum*, 1995]. Dissipation ε is estimated from shear microstructure measurements on timescales of seconds, derived from velocity fluctuations of the same timescale $\boldsymbol{u}'$. Quantities averaged over that turbulence timescale are denoted by an overbar:

$$\overline{\boldsymbol{S}} = \boldsymbol{S}_0 + \widetilde{\boldsymbol{S}}. \tag{2}$$

[37] Having split the momentum equation into turbulence and averaged parts, one easily arrives at the turbulence kinetic energy equation. Introducing the assumption that the

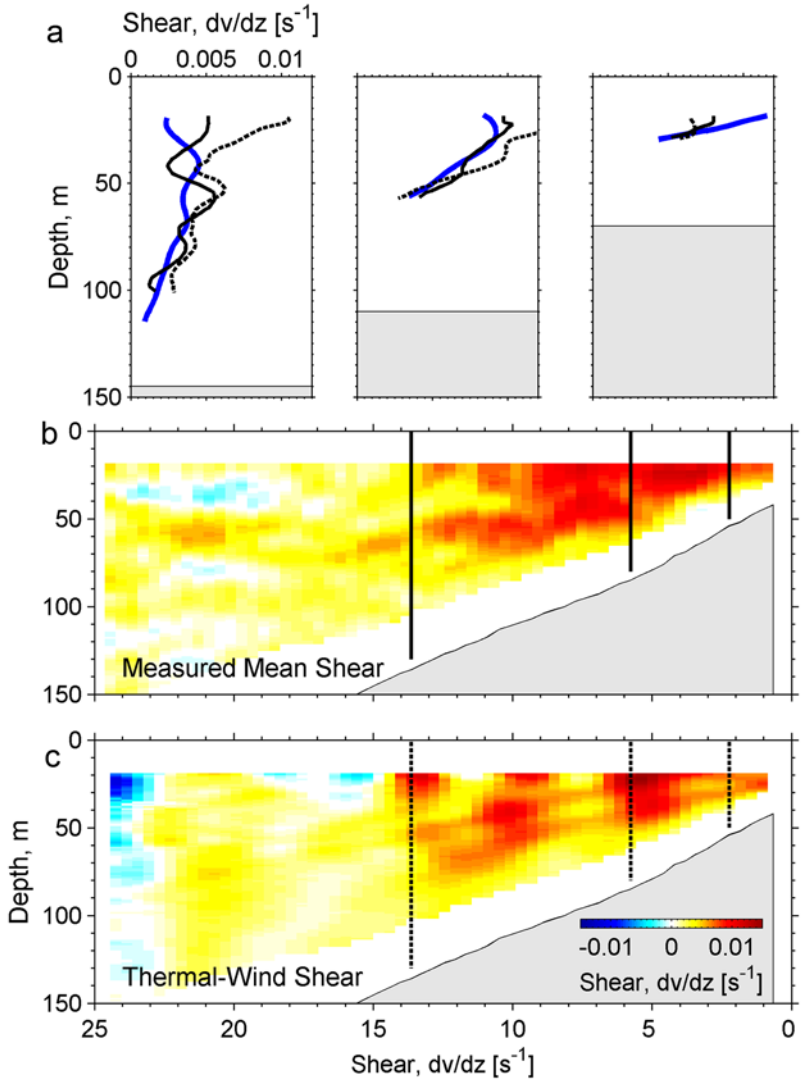

Figure 9. (a) PWA low-frequency shear estimate ${}^{S}\boldsymbol{S}_0$ (solid black lines), data taken from the thermal wind estimate ${}^{T}\boldsymbol{S}_0$ (dashed black lines), and low-frequency shear measured at each mooring ${}^{M}\boldsymbol{S}_0$ (solid blue lines). (b and c) Two contour maps, both of which portray low-frequency along-shelf shear estimates. Figure 9b shows estimate calculated directly from shear observations using the phase-weighted mean ${}^{S}\boldsymbol{S}_0$. Figure 9c shows estimate calculated from thermal wind balance of the low-frequency density field ${}^{T}\boldsymbol{S}_0$. The two estimates are compared directly at three locations (vertical lines), which correspond to the locations of the the three across-shore moorings.

turbulence is nearly steady state and turbulent advection is small,

$$P = B + \varepsilon, \tag{3}$$

where P and B represent the turbulence shear production and buoyancy production terms, respectively. For a turbulence energy balance as written in equation (3), eddy viscosity is estimated [*Dillon et al.*, 1989] as

$$K_V = \frac{(1+\Gamma)\varepsilon}{|\boldsymbol{S}|^2}, \tag{4}$$

where the mixing efficiency Γ is the ratio of the work done in increasing the potential energy of the system compared to that dissipated by viscosity: We use a typical oceanic value of 0.2 here [*Peltier and Caulfield*, 2003]. The denominator of equation (4) is the square of the shear of the averaged velocity field which we now expand into the thermal wind and IGW components:

$$K_V = \frac{(1+\Gamma)\varepsilon}{\left(\left|\boldsymbol{S}_0 + \widetilde{\boldsymbol{S}}\right|\right)^2}. \tag{5}$$

Finally, turbulence stress $\boldsymbol{\tau}$ is defined as simply the product of K_V and the shear of the averaged velocity:

$$\boldsymbol{\tau} = K_V \rho \overline{\boldsymbol{S}} = \frac{(1+\Gamma)\varepsilon}{\left(\left|\boldsymbol{S}_0 + \widetilde{\boldsymbol{S}}\right|\right)^2}\left(\boldsymbol{S}_0 + \widetilde{\boldsymbol{S}}\right). \tag{6}$$

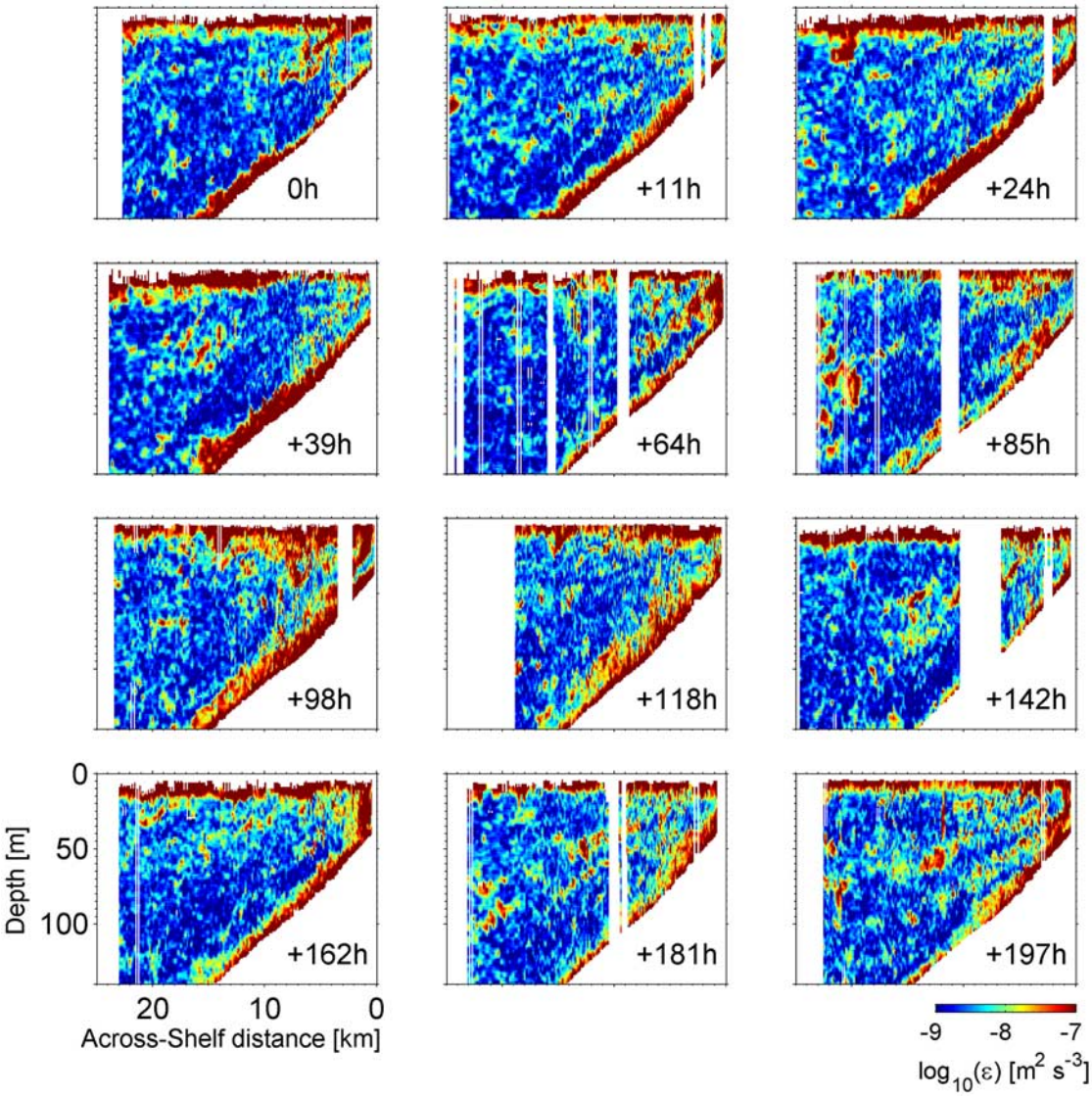

Figure 10. Observed cross-shelf dissipation sections for each of the 12 transects conducted. The first transect is shown at the top left, moving sequentially to the right and down. Values in the bottom and surface mixed layers are typically higher than 10^{-7}, and are therefore saturated.

[38] Equations (5) and (6) are estimates of the eddy viscosity and turbulent stress in the averaged momentum equations, where that averaging is on timescales long compared to turbulent timescales. In the context of the three-scale decomposition of equation (1) we wish to average this equation again, separating fluctuations on the timescales of the IGWs field from that of the "low-frequency" thermal wind jet. Again, within this study that averaging was defined as the 9-day average, for which we used angle brackets to denote, such that $\boldsymbol{S}_0 = \langle \boldsymbol{S} \rangle$. As all the microstructure data were obtained from shipboard Chameleon measurements, this averaging processis necessarily performed using the PWA in the same manner as discussed previously:

$$K_{V0} = \left\langle \frac{(1+\Gamma)\varepsilon}{\left(\boldsymbol{S}_0 + \tilde{\boldsymbol{S}}\right)^2} \right\rangle_{\mathrm{PWA}}. \tag{7}$$

[39] K_{V0} ranges from 10^{-5} to 10^{-4} m^2 s^{-1} in the core of the jet. The cross-shelf structure of τ_0^y is shown in Figure 13 (right); τ_0^y is large within the region of thermal wind shear, with near-zero values offshore; for comparison, ε_0 (Figures 12a and 12c) is also shown; τ_0^y is largest at the base of the upwelling jet inside the 100-m isobath (with a value of $\sim 10^{-7}$ W kg^{-1}), coincident with the location of maximum thermal wind shear (contours, Figure 13). A significant correlation (r = 0.42–95% confidence interval [0.40–0.45]) is found between ${}^{S}S_0^y$ and $\log_{10}(\varepsilon_0)$: ε_0 tends to be highest where the upwelling jet shear is also large.

[40] The vertical divergence of turbulence stress acts to accelerate/decelerate the local flow

$$\frac{\partial v}{\partial t} \propto \frac{1}{\rho_0}\frac{\partial \tau^y}{\partial z}. \tag{8}$$

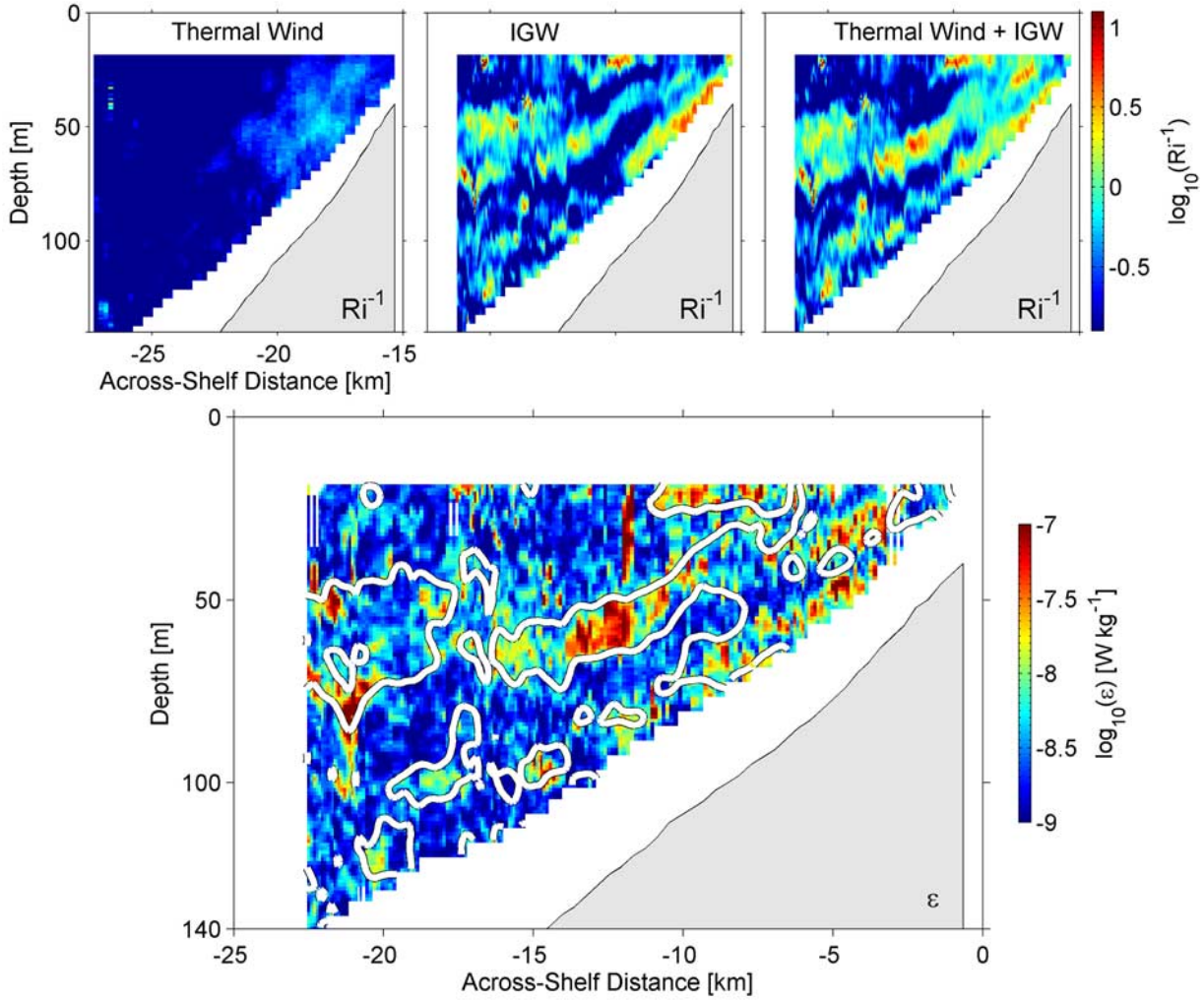

Figure 11. Richardson number dissipation comparison for transect +197 hours. (top) Three images maps of a Richardson number quantity $\log_{10}(Ri^{-1})$, such that positive values (yellow-red) correspond to unstable Ri^{-1} and negative values (blues) indicate stable Ri^{-1}. (left) Ri^{-1} calculated from the thermal wind shear alone, (middle) Ri^{-1} calculated from the IGW shear alone, and (right) Ri^{-1} from the total shear field. (bottom) Plot of $\log_{10}(\varepsilon)$ for the same transect. Note the qualitative correspondence between the observed dissipation and regions of elevated Ri^{-1}, with a contour (white) which delineates a mask in which $Ri^{-1} > 1$.

Differentiation of equation (8) with depth reveals that the curvature of the stress profile produces time rate of change of the vertical shear profile:

$$\frac{\partial S^v}{\partial t} \propto \frac{1}{\rho_0}\frac{\partial^2 \tau^v}{\partial z^2}. \tag{9}$$

[41] Using equation (9), we estimate the impact of τ_0^v on the thermal wind jet. While this quantity is noisy, there is clearly a band of elevated τ_0^v at middepth; the mean profile contains a maximum in τ_0^v near the center of the water column, colocated with the region of maximum shear in the thermal wind jet (Figure 14). (The mean profile was calculated from profiles in a 10-km swath, centered at the 100-m isobath.) The convex curvature associated with this profile is negative, indicating that the effect of the turbulent stress is to decrease S_0^v with time. We employ a second-order polynomial fit over a selected region of a spatially averaged profile of τ_0^v (between x = 5 km and x = 15 km) to estimate the curvature. The fit was performed across data that fall between water depths of 40 and 70 m, chosen as the region over which the thermal wind shear is a maximum. (This fit is chosen as a reasonable estimate of the curvature associated with the midwater maximum in stress shown in Figure 12. The minimum bound on stress curvature would be that associated with the fit from surface to bottom, while the maximum would be the curvature associated with the peak found at ~50-m depth (Figure 13). We chose the discussed fit on the basis of the width of the peak in thermal wind shear, also found at ~50 m (but with a considerably wider profile) as a reasonable estimate of the curvature associated with the stress found at the peak of the thermal

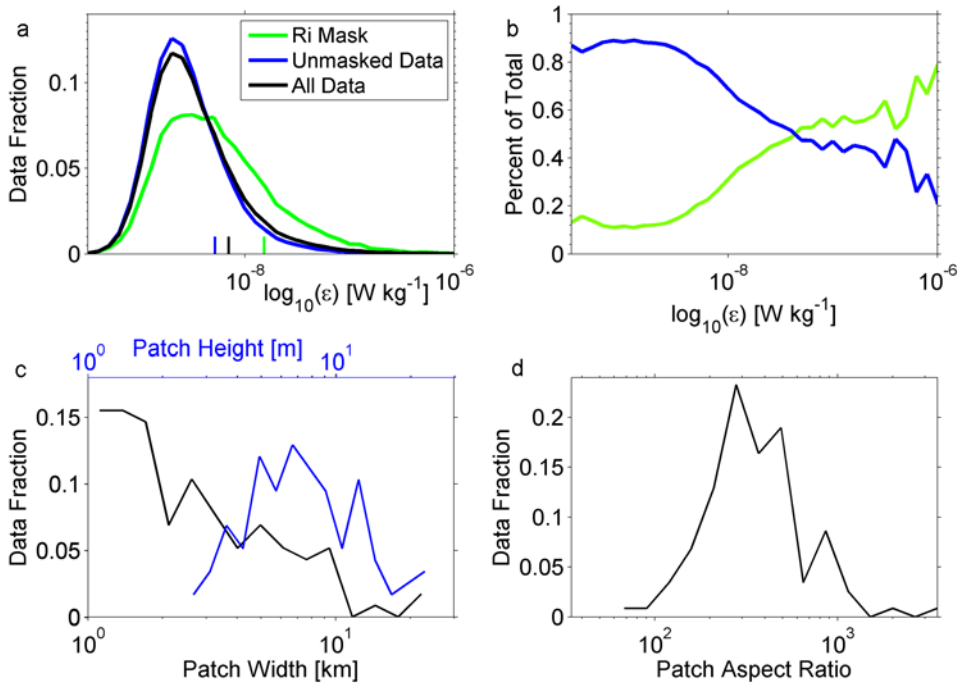

Figure 12. Statistics associated with the masking routines used to identify dissipation patches. (top left) Normalized histograms of ε for various subsets of data. Also shown are the mean values of dissipation for each subset, marked by small vertical lines along the abscissa. (top right) Percent of total dissipation values in each bin included within each subset. (bottom left) Histograms of patch width (maximum across-shore extent of each patch) (black line) and patch height (average height of each patch) (blue line). (bottom right) Histogram of patch aspect ratio.

wind shear layer. Given the range of reasonable estimates of curvature in the stress, this temporal estimate is likely to be accurate within a factor of ~3.)

[42] A decay timescale associated with changes in shear magnitude can be estimated using the fit to the turbulence stress profile. Fitting to the region of maximum velocity shear between 20 and 50-m depth (dashed black line) results in $[(1/\rho_0)(\partial^2\tau/\partial z^2)] \approx 4 \times 10^{-9}$ s^{-2}. This value is consistent with the fact that the thermal wind jet is geostrophic to first order, as the magnitude of the geostrophic terms in this flow is $fS_0^y \approx 5 \times 10^{-7}$ s^{-2} or 2 orders of magnitude larger than the turbulent stress curvature. While the jet is most certainly in near-geostrophic balance, the turbulent stress divergence is significant in the second-order force balance. In the absence of any additional energy input (removal of the surface wind stress) the spin-down time of the geostrophic shear from internal turbulent stress is Δt = O(10) days.

[43] *Lentz and Chapman* [2004] note that the cross-shelf momentum flux divergence term becomes important as the slope Burger number of a shelf increases. A typical value of the slope Burger number for the Oregon shelf during summer is ~1.0 based on a buoyancy frequency of ~0.02, f of ~10^{-4}, and a bottom slope of ~0.005. For such a value, Lentz and Chapman's results suggest that the cross-shelf return flow should be distributed throughout the interior of the water column, a finding somewhat at odds with studies of the bottom boundary layer (BBL) on the Oregon coast [*Perlin et al.*, 2005b, 2007] which find that the bottom Ekman layer and its transport are largely confined to the bottom (~5–10 m thick). We find that the observed turbulent stress in the interior of the flow (e.g., Figure 14) is small compared to typical values of the surface wind stress (e.g., 1×10^{-4} m^2 s^{-2} [*Lentz and Chapman*, 2004]).

4.2. Enhanced Coastal Mixing

[44] Irreversible mixing affects any scalar within the coastal waters, including both dynamically important (temperature and salinity) and biologically important (e.g., dissolved oxygen) scalars. As a particularly relevant example, *Hales et al.* [2005] examined nitrate flux off Oregon's coast. They found that the flux of nitrate from near-bottom to near-surface waters due to turbulent mixing was approximately 1/4 of the total transport: a significant and irreversible contributor to the nitrate flux which plays a significant role to the high-productivity seen on the shelf. (The remaining 3/4 of the total nitrate flux to surface waters was contributed directly by Ekman transport.)

[45] Enhanced mixing may be indirectly important to the dynamics of the thermal wind shear by mixing the temperature and salinity fields which support the cross-shelf pressure gradient [e.g., *Dewey and Moum*, 1990]. The 9-day mean eddy diffusivity is defined as [*Osborn*, 1980]

$$K_{\rho 0} = \left\langle \frac{\Gamma \varepsilon}{N^2} \right\rangle_{\mathrm{PWA}}. \tag{10}$$

Values of $K_{\rho 0}$ resulting from equation (10) are at least 5 orders of magnitude above molecular diffusivity of salt, over the entire cross section. To illustrate the result of this

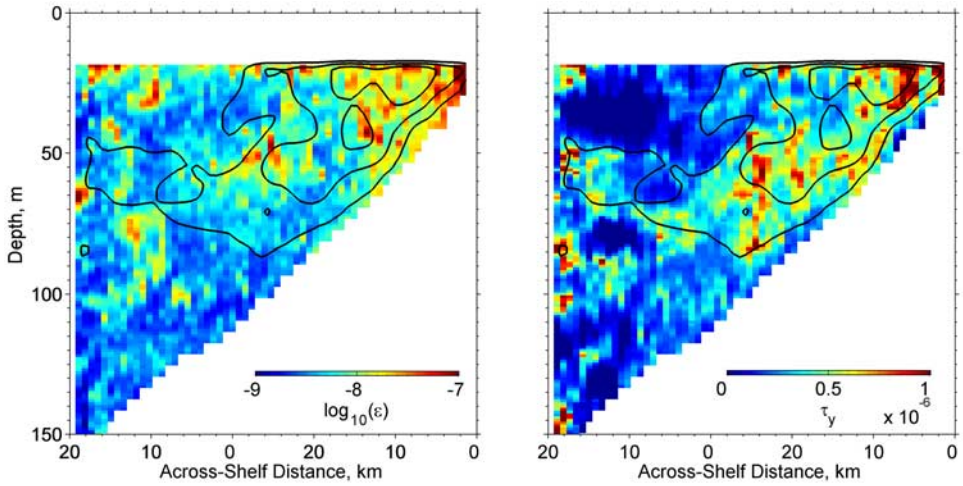

Figure 13. (left) Mean dissipation cross section ε_0. (right) Along-shelf turbulent stress estimate τ_o^y. Averages were computed using the phase-weighted averaging technique described in text. Also plotted are contours of the low-frequency along-shelf shear.

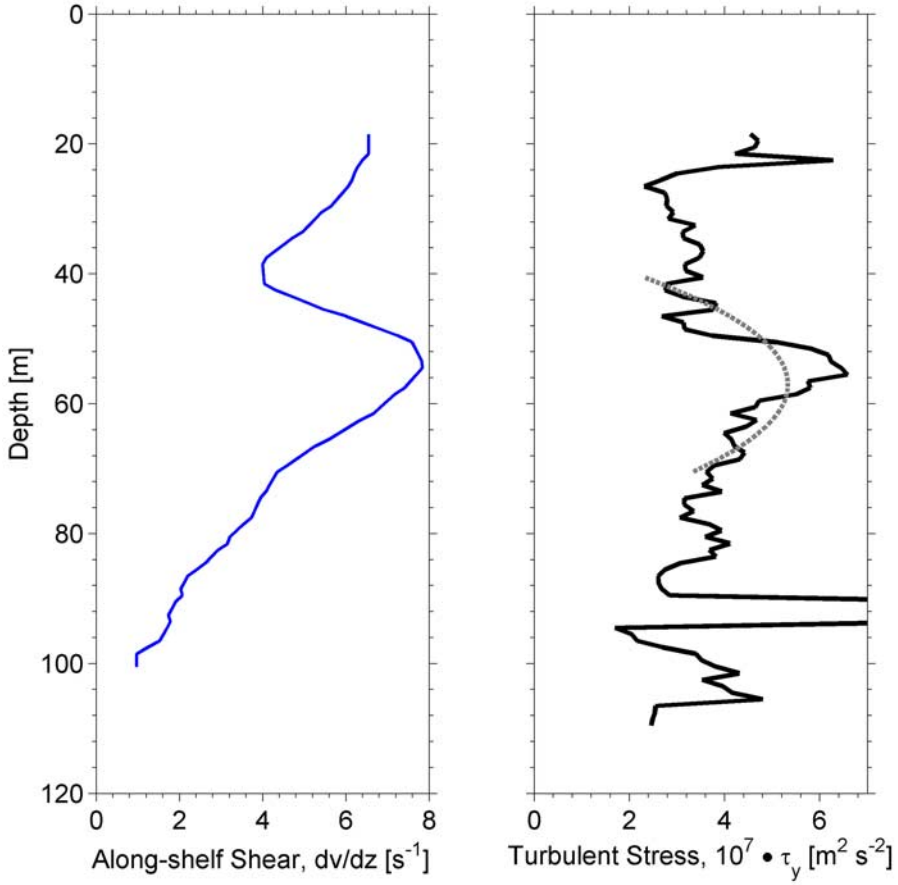

Figure 14. Comparison between (left) thermal wind shear estimate dv/dz and (right) low-frequency turbulent stress τ_o^y. Both the shear and the turbulent stress are an along-shelf average of profiles centered at between $x = 5$ km and $x = 15$ km. A second-order polynomial is fit to the observed curvature in the turbulent stress (dashed black curve). The region fit to the polynomial corresponds to the region in which the thermal wind shear is a maximum, between 40-m and 70-m depth. The curvature of the fit is an overestimate of the curvature of the water column from top to bottom, but it is clearly an underestimate of the curvature associated with the peak of the thermal wind shear.

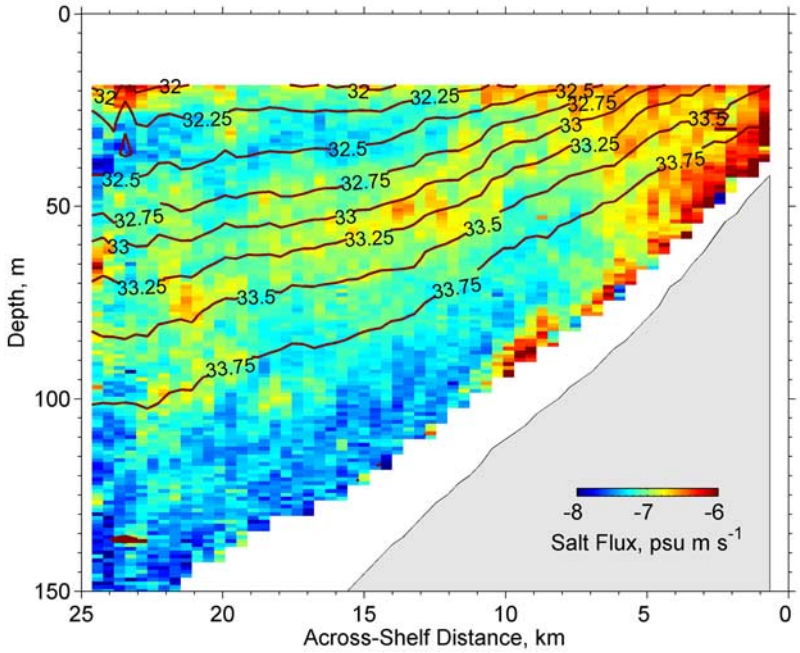

Figure 15. PWA salt flux calculated over the 9-day period. All values correspond to upward flux of salt. Also shown are the isohalines corresponding to the PWA salinity structure for the experiment.

enhanced diffusivity, we employ Chameleon's observations of salinity *Sa* to calculate the salt flux:

$$F_{Sa} = \left\langle K_\rho \frac{dSa}{dz} \right\rangle_{\mathrm{PWA}}. \tag{11}$$

[46] The turbulence driven salt flux is most significant inside the 100 m isobath ($\sim 10^{-6}$ practical salinity units (psu) m s^{-1}, Figure 15) where F_{Sa} exceeds that outside this turbulent "core" by more than an order of magnitude. Offshore of this region, we observe a band of high salt flux near the base of the isopycnal structure associated with the upwelling jet ($\sim 10^{-7}$ psu m s^{-1}). This band also has significantly elevated salt flux, albeit slightly less than that present in the core. Although the salt flux is particularly large along the base of the jet, we note that the salt stratification is not particularly large in this location (as shown by the isohaline contours). Instead, this band of elevated flux is driven by the enhanced turbulence (as suggested by the stress profile in Figure 14). Both the salt flux found inshore of the 100-m isobath and that along the base of upwelling jet offshore of that location are many orders of magnitude higher than that predicted by "background" eddy diffusivity of numerical models acting upon the same salinity gradient.

[47] We compare this to the salt transported by advection toward the coast by the upwelling circulation. Assuming a value of F_{Sa} along the bottom of the upwelling jet of $\sim 5 \times 10^{-7}$ psu m s^{-1} across a 30-km-wide shelf, there is an upward salt transport of 0.006 psu m^2 s^{-1}. During upwelling season, dense salty fluid is being advected toward shore in the bottom mixed layer, while simultaneously mixed upward via the turbulence. From CHAMELON profiles we estimate that the salt differential ΔSa between the bottom boundary layer and the coastal environment above is typically $\sim$0.5 psu. To balance this upward salt transport, the average transport in the BBL must therefore be $\sim$0.03 m^2 s^{-1}. *Perlin et al.* [2005a] estimated the transport within the BBL by tracking the movement of isopycnals over a 9-day period. Typical BBL thickness was $\sim$10 m, requiring an average BBL velocity $\sim$0.003 m s^{-1} ($\sim$300 m d^{-1}) onshore. In comparison, *Perlin et al.* [2005a] observed BBL velocities ranging from 6 km d^{-1} (onshore) to -4 km d^{-1} (offshore) over the study period.

[48] Dynamically, an enhanced vertical transport of salt (combined with a similar enhanced transport of heat) should result in a significantly weakened cross-shelf density gradient and likewise a weakened thermal wind shear. If mixing were significantly reduced (for instance, if the IGW field were absent) in the midwater coastal ocean, the only strong surface-to-bottom transport will occur very near the shore where the surface mixed layer (SML) and BBL merge. In this case, the salt advected onshore in the bottom Ekman layer will tend to be transported farther onshore, producing a saltier coastal ocean near-shore, with stronger density gradients.

5. Summary and Conclusions

[49] The major results of this study are summarized as follows:

[50] 1. Three primary contributors to the shear are the slowly varying thermal wind, the M_2 internal tide, and near-*f* waves, all of which were of similar magnitude, with the thermal wind shear being approximately a factor of 2 less than the magnitude of the higher-frequency fluctuations.

[51] 2. The M_2 internal tide was found to dominate the internal wave signal near shore, while the near-*f* band was

found to be more important offshore. The IGW shear magnitude was found to be larger, on average, in locations at which the thermal wind shear was also larger. This correspondence effectively concentrates the largest values of both shear components at the base of the upwelling jet where the largest values of (average) dissipation are also observed. We are unable to determine if this effect is simply due to the presence of increased density gradient in the same region or if there is nonlinear interaction between the two signals that contributes.

[52] 3. Sheets of elevated dissipation are found to be colocated with regions of large inverse Richardson number. Continuous regions (referred to as patches) were located, and statistics on these patches were computed. The patches were found to be typically ~10 m in height and many kilometers in cross-shelf width. Elevated dissipation values are most densely concentrated inshore of the 100-m isobath colocated with the region of maximum thermal wind shear.

[53] 4. The mean turbulent stress was calculated via the weighted averaging technique used to resolve the low-frequency shear from shipboard observations. The stress divergence is found to be of secondary importance in the momentum balance. The spin-down timescale of the geostrophic shear (isopycnal flattening) due to the turbulent stress is ~2 weeks.

[54] 5. Most importantly, it is demonstrated that the enhanced turbulence greatly increases the turbulent diffusivity within the upwelling jet. It was found that values of turbulent diffusivity are increased 5 to 6 orders of magnitude above molecular in the case of salt. Using the salt flux estimates calculated from this study, we find that the necessary salt transport in the bottom boundary layer from Ekman dynamics is consistent with observations. The enhanced on-shelf turbulent mixing therefore produces scalar transports consistent with the salt flux driven by the midshelf turbulence. This enhanced coastal mixing via turbulent transport is clearly important to the ecology of the shelf [e.g., *Hales et al.*, 2005], in that a whole host of biologically relevant scalars are affected by the magnitude of the vertical turbulent transport.

[55] **Acknowledgments.** This work was funded by the National Science Foundation (grant 9907854). We gratefully acknowledge the work of Jody Klymak, Mike Neely-Brown, Ray Kreth, Grieg Thomson, and the crew of the R/V *Thomas G. Thompson* for their contributions to Chameleon and in collecting the data. Thanks also to Walt Wardorf, Tim Boyd, Mike Kosro, and Steve Gard for their role in deploying the moorings and processing the data.

References

Anis, A., and J. N. Moum (1995), Surface wave-turbulence interactions: Scaling $\varepsilon(z)$ near the sea surface, *J. Phys. Oceanogr.*, *25*, 2025–2045.

Barth, J. A., and P. A. Wheeler (2005), Introduction to special section: Coastal advances in shelf transport, *J. Geophys. Res.*, *110*, C10S01, doi:10.1029/2005JC003124.

Barth, J. A., S. D. Pierce, and R. M. Castelao (2005), Time-dependent, wind-driven flow over a shallow mid shelf submarine bank, *J. Geophys. Res.*, *110*, C10S05, doi:10.1029/2004JC002761.

Boyd, T., M. D. Levine, P. M. Kosro, S. R. Gard, and W. Waldorf (2002), Observations from moorings on the Oregon continental shelf, May–August 2001, *Data Rep. 190*, *Ref. 02-6*, Coll. of Oceanic and Atmos. Sci., Oreg. State Univ., Corvallis.

Chriss, T. M., and D. R. Caldwell (1982), Evidence for the influence of form drag on bottom boundary layer flow, *J. Geophys. Res.*, *87*, 4148–4154.

Denbo, D. W., and J. S. Allen (1984), Rotary empirical orthogonal function analysis of currents near the Oregon coast, *J. Phys. Oceanogr.*, *14*, 35–46.

Dewey, R. K., and W. R. Crawford (1988), Bottom stress estimates from vertical dissipation rate profiles on the continental shelf, *J. Phys. Oceanogr.*, *18*, 1167–1177.

Dewey, R. K., and J. N. Moum (1990), Enhancement of fronts by vertical mixing, *J. Geophys. Res.*, *95*(C6), 9433–9445.

Dewey, R. K., J. N. Moum, and D. R. Caldwell (1993), Microstructure activity within a minifilament in the coastal transition zone, *J. Geophys. Res.*, *98*, 14,457–14,470.

Dillon, T. M., J. N. Moum, T. K. Chereskin, and D. R. Caldwell (1989), Zonal momentum balance at the equator, *J. Phys. Oceanogr.*, *19*, 561–570.

Garvine, R. W. (1999), Penetration of buoyant coastal discharge onto the continental shelf: A numerical experiment, *J. Phys. Oceanogr.*, *29*, 1892–1909.

Hales, B., J. N. Moum, P. Covert, and A. Perlin (2005), Irreversible nitrate fluxes due to turbulent mixing in a coastal upwelling system, *J. Geophys. Res.*, *110*, C10S11, doi:10.1029/2004JC002685.

Huyer, A. (1983), Coastal upwelling in the California Current System, *Prog. Oceanogr.*, *12*, 259–284.

Huyer, A., R. L. Smith, and R. D. Pillsbury (1972), Observations in a coastal upwelling region during a period of variable winds (Oregon coast, July 1972), *Tethys*, *6*, 391–404.

Huyer, A., R. L. Smith, and E. J. Sobey (1978), Seasonal differences in low-frequency current fluctuations over the Oregon continental shelf, *J. Geophys. Res.*, *83*, 5077–5089.

Huyer, A., E. J. Sobey, and R. L. Smith (1979), The spring transition in currents over the Oregon continental shelf, *J. Geophys. Res.*, *84*, 6995–7011.

Klymak, J. M., and J. N. Moum (2003), Internal solitary waves of elevation advancing on a shoaling shelf, *Geophys. Res. Lett.*, *30*(20), 2045, doi:10.1029/2003GL017706.

Kurapov, A. L., J. S. Allen, G. D. Egbert, R. N. Miller, P. M. Kosro, M. D. Levine, T. Boyd, and J. A. Barth (2005), Assimilation of moored velocity data in a model of coastal wind-driven circulation off Oregon: Multivariate capabilities, *J. Geophys. Res.*, *110*, C10S08, doi:10.1029/2004JC002493.

Lentz, S. J., and D. C. Chapman (2004), The importance of nonlinear cross-shelf momentum flux during wind-driven coastal upwelling, *J. Phys. Oceanogr.*, *34*, 2444–2457.

Levine, M. D. (2002), A modification of the Garret-Munk internal wave spectrum, *J. Phys. Oceanogr.*, *32*, 3166–3181.

MacKinnon, J. A., and M. C. Gregg (2003a), Shear and baroclinic energy flux on the summer New England shelf, *J. Phys. Oceanogr.*, *33*, 1462–1475.

MacKinnon, J. A., and M. C. Gregg (2003b), Mixing on the late-summer New England shelf-solibores, shear and stratification, *J. Phys. Oceanogr.*, *33*, 1476–1492.

MacKinnon, J. A., and M. C. Gregg (2005a), Near-inertial waves on the New England shelf: The role of evolving stratification, turbulent dissipation, and bottom drag, *J. Phys. Oceanogr.*, *35*, 2408–2424.

MacKinnon, J. A., and M. C. Gregg (2005b), Spring mixing: Turbulence and internal waves during restratification on the New England shelf, *J. Phys. Oceanogr.*, *35*, 2425–2443.

Moum, J. N., and J. D. Nash (2000), Topographically induced drag and mixing at a small bank on the continental shelf, *J. Phys. Oceanogr.*, *30*, 2049–2054.

Moum, J. N., and W. D. Smyth (2006), The pressure disturbance of a nonlinear internal wave train, *J. Fluid Mech.*, *558*, 153–177.

Moum, J. N., M. C. Gregg, R. C. Lien, and M. E. Carr (1995), Comparison of turbulence kinetic energy dissipation rate estimates from two ocean microstructure profilers, *J. Atmos. Oceanic Technol.*, *12*, 346–366.

Moum, J. N., D. M. Farmer, W. D. Smyth, L. Armi, and S. Vagle (2003), Structure and generation of turbulence at interfaces strained by internal solitary waves propagating shoreward over the continental shelf, *J. Phys. Oceanogr.*, *33*, 2093–2112.

Moum, J. N., J. M. Klymak, J. D. Nash, A. Perlin, and W. D. Smyth (2007a), Energy transport by nonlinear internal waves, *J. Phys. Oceanogr.*, in press.

Moum, J. N., D. M. Farmer, E. L. Shroyer, W. D. Smyth, and L. Armi (2007b), Dissipative losses in nonlinear internal waves propagating across the continental shelf, *J. Phys. Oceanogr.*, in press.

Nash, J. D., and J. N. Moum (2001), Internal hydraulic flows on the continental shelf: High drag states over a small bank, *J. Geophys. Res.*, *106*, 4593–4612.

Osborn, T. R. (1980), Estimates of the local rate of vertical diffusion from dissipation measurements, *J. Phys. Oceanogr.*, *10*, 83–89.

Peltier, W. R., and C. P. Caulfield (2003), Mixing efficiency in stratified sheared flows, *Annu. Rev. Fluid Mech.*, *35*, 135–167.

Perlin, A., J. N. Moum, and J. M. Klymak (2005a), Response of the bottom boundary layer over a sloping shelf to variations in alongshore wind, *J. Geophys. Res.*, *110*, C10S09, doi:10.1029/2004JC002500.

Perlin, A., J. N. Moum, J. M. Klymak, M. D. Levine, T. Boyd, and P. M. Kosro (2005b), A modified law-of-the-wall applied to oceanic bottom boundary layers, *J. Geophys. Res.*, *110*, C10S10, doi:10.1029/2004JC002310.

Perlin, A., J. N. Moum, J. M. Klymak, M. D. Levine, T. Boyd, and P. M. Kosro (2007), Organization of stratification, turbulence, and veering in bottom Ekman layers, *J. Geophys. Res.*, *112*, C05S90, doi:10.1029/2004JC002641.

Rippeth, T. P., N. R. Fisher, and J. H. Simpson (2001), The cycle of turbulent dissipation in the presence of tidal straining, *J. Phys. Oceanogr.*, *31*, 2458–2471.

Sanford, T. B., and R.-C. Lien (1999), Turbulent properties in a homogeneous bottom tidal boundary layer, *J. Geophys. Res.*, *104*, 1245–1257.

Torgrimson, G. M., and B. M. Hickey (1978), Barotropic and baroclinic tides over the continental slope and shelf off Oregon, *J. Phys. Oceanogr.*, *9*, 945–961.

Winkel, D. P., M. C. Gregg, and T. B. Sanford (2002), Patterns of shear and turbulence across the Florida Current, *J. Phys. Oceanogr.*, *32*, 3269–3282.

G. S. Avicola, Applied Physics Laboratory, Johns Hopkins University, 11100 Johns Hopkins Road, Laurel, MD 20723, USA. (gavicola@comcast.net)

M. D. Levine, J. N. Moum, and A. Perlin, College of Oceanic and Atmospheric Sciences, Oregon State University, 104 COAS Administration Building, Corvallis, OR 97331-5503, USA.